

Spiral arms, bar shape and bulge microlensing in the Milky Way

Nicolai Bissantz¹ and Ortwin Gerhard¹

¹*Astronomisches Institut der Universität Basel, Venusstr.7, CH-4102 Binningen*

6 November 2018

ABSTRACT

A new model for the luminosity distribution in the inner Milky Way is found, using a non-parametric penalized maximum-likelihood algorithm to deproject a dereddened *COBE/DIRBE* L-band map of the inner Galaxy. The model is also constrained by the apparent magnitude (line-of-sight) distributions of clump giant stars in certain bulge fields. An important new feature is the inclusion of a spiral arm model in the disk.

Spiral arms make the model appear broader on the sky, thus our bar is more elongated than in previous eight-fold symmetric models. They also lead to a smoother disk model interior to the Sun. The bar length is ≈ 3.5 kpc and its axis ratios are 1:(0.3–0.4):0.3, independent of whether the spiral arm model is 4-armed or 2-armed. The larger elongation in the plane makes it possible to reproduce the observed clump giant distributions as well. With only the surface brightness data a small model degeneracy is found even for fixed orientation of the bar, amounting to about ± 0.1 uncertainty in the in-plane axial ratio. Including the clump giant data removes most of this degeneracy and also places additional constraints on the bar’s orientation angle. We estimate $15 \text{ deg} \lesssim \varphi_{\text{bar}} \lesssim 30 \text{ deg}$, with the best models obtained for $20 \text{ deg} \lesssim \varphi_{\text{bar}} \lesssim 25 \text{ deg}$.

We use our reference model to predict a microlensing optical depth map towards the bulge, normalising its mass by the observed terminal velocity curve. For clump giant sources at $(l, b) = (3.9 \text{ deg}, -3.8 \text{ deg})$ we find $\tau_{-6} \equiv \tau/10^{-6} = 1.27$, within 1.8σ of the new MACHO measurement given by Popowski et al. The value for all sources at $(l, b) = (2.68 \text{ deg}, -3.35 \text{ deg})$ is $\tau_{-6} = 1.1$, still $> 3\sigma$ away from the published MACHO DIA value. The dispersion of these τ_{-6} values within our models is $\simeq 10\%$. Because the distribution of sources is well-fit by the NIR model, increasing the predicted optical depths by $> 20\%$ will be difficult. Thus the high value of the measured clump giant optical depth argues for a near-maximal disk in the Milky Way.

Key words: Galaxy: structure - Galaxy: centre - Galaxies: spiral.

1 INTRODUCTION

Observations of the Milky Way [MW] show significant systematic differences between the NIR surface brightness of the MW at $l > 0 \text{ deg}$ and $l < 0 \text{ deg}$ (e.g., Blitz & Spergel (1991), Weiland et al. (1994), Bissantz et al. (1997)). It is widely accepted that these variations reflect the fact that the MW is a barred spiral galaxy. Evidence for a barred component of the luminosity density in the inner MW also comes from starcount observations (e.g., Stanek et al. (1997), Nikolaev & Weinberg (1997), Sevenster (1999), Hammersley et al. (1999), López-Corrodoira et al. (2000)), from gas-dynamics (e.g., Englmaier & Gerhard (1999), Fux (1999), Weiner & Sellwood (1999)), and microlensing observations (e.g., Paczynski et al. (1994), Zhao, Rich & Spergel (1996)). Further references can be found in Gerhard ((2001)).

The starcount data show significant asymmetries between lines-of-sight that are symmetrical with respect to the $l = 0$ axis; this is the signature of a bar with its near end at positive Galactic longitudes. Most importantly, starcount data contain information about the distances to the surveyed stars. This is complementary to the all-sky coverage of surface brightness maps, and is valuable for constraining the line-of-sight structure of the bulge even if available only for a restricted number of fields. In this paper we will take one step towards combining the information from both kinds of data, and use the clump giant observations of Stanek et al. ((1994), (1997)) together with the *COBE/DIRBE* NIR data to determine a model for the luminosity distribution in the inner Galaxy. With this model we can be more confident about the line-of-sight distribution (LOS) of microlensing sources, and are thus in a much better position to predict mi-

crowding optical depths for comparison with the recent determinations from the MACHO group (Alcock et al. (2000a), Popowski et al. (2000)).

Most previous models of the inner MW have been parametric and are thus restricted towards certain classes of densities for the bulge and/or disk. Binney & Gerhard (1996) developed a nonparametric approach to the deprojection of the *COBE/DIRBE* data based on the Richardson-Lucy algorithm, in which by construction the luminosity models are eight-fold symmetric with respect to the three main planes of the bar/bulge. Models constructed with this approach (Binney et al. (1997); Bissantz et al. (1997)) give a good fit to the *COBE/DIRBE* L-band data, but predict less asymmetric LOS distributions towards the fields observed by Stanek et al. (1994) than observed, by more than 0.1^m . Eight-fold symmetry also excludes modeling the spiral arms of the MW (see, e.g., Englmaier & Gerhard (1999), Drimmel & Spergel (2001)). In the present paper we describe a non-parametric penalized likelihood approach to infer the luminosity density of the inner MW from the *COBE/DIRBE* data which allows us to include a spiral arm model.

This paper is organized as follows. Section 2 describes our new deprojection algorithm. In Section 3 we test the method with known parametric distributions and analyse the uniqueness of the deprojected bar shape. In Section 4 we present models for the luminosity distribution of the MW which are consistent with both the *COBE/DIRBE* L-band data and the observed asymmetry in the distribution of clump giant stars, and give constraints on the orientation angle of the Galactic bar. In Section 5 we predict the microlensing optical depths for these models and compare to recently published results of the MACHO experiment. We close with a summary and conclusions in Section 6.

2 MAXIMUM LIKELIHOOD DEPROJECTION METHOD

In this Section we describe the technique we have used to construct models for the Milky Way's luminosity distribution. It is a non-parametric technique that maximizes a likelihood function, which includes penalty terms encouraging smoothness, eight-fold (triaxial) symmetry and a spiral arm component in the model. The minimisation procedure is iterative, starting from an initial parametric model. The following subsections describe the initial parametric models (§2.1), the algorithm (§2.2), the choice of optimal penalty parameters (§2.3) and the performance of the algorithm (§2.4). The results of using the algorithm to recover known solutions from artificial data are described in §3.

2.1 Parametric models

We define parametric models for the luminosity distribution of the MW on a cartesian grid. The coordinate system has the Galactic centre at its origin. The axes are parallel to the main axes of the bar. In this coordinate system the position of the Sun is $(x = R_0 \cos(\varphi_{\text{bar}}), y = R_0 \sin(\varphi_{\text{bar}}), Z_0)$, where R_0 is the distance of the Sun from the Galactic centre projected onto the main plane of the Milky Way, Z_0 the position of the Sun above the xy -plane, and φ_{bar} the ‘‘bar angle’’, i.e., the angle in the xy -plane between the major axis of the bar

and the projected line-of-sight from the Sun to the Galactic centre, such that for positive φ_{bar} the near end of the bar is at positive longitudes. Throughout this paper we will use $R_0 = 8$ kpc and $Z_0 = 14$ pc.

Our parametric models contain a double-exponential disk and a truncated power-law bulge (cf. Binney, Gerhard & Spergel (1997)):

$$\hat{\rho}(\vec{x}) = \rho_d(\vec{x}) + \rho_b(\vec{x}), \quad (1)$$

where

$$\rho_d \equiv \rho_d^0 \cdot R_d \cdot e^{-R/R_d} \cdot \left(\frac{e^{-|z|/z_0}}{z_0} + \alpha \frac{e^{-|z|/z_1}}{z_1} \right),$$

$$\rho_b \equiv \frac{\rho_b^0}{\eta \zeta a_m^3} \cdot \frac{e^{-a^2/a_m^2}}{(1 + a/a_0)^{1.8}},$$

$$a \equiv \sqrt{x^2 + \frac{y^2}{\eta^2} + \frac{z^2}{\zeta^2}}, \quad R \equiv \sqrt{x^2 + y^2} \quad \text{and} \quad \vec{x} = (x, y, z).$$

In some models we also include an additional spiral arm component. This is taken from Ortiz & Lépine (1993), who obtained a good fit to the tangent directions seen in infrared star counts with four logarithmic spirals. See Table 1 of Englmaier & Gerhard (1999) for other tracers of these tangent directions. The positions of the spiral arms $r_i(\phi)$ ($i = 1, \dots, 4$) are given by

$$r_i(\phi) = 2.33 \text{ kpc} \cdot e^{(\phi - \varphi_{\text{bar}} - \phi_i) \cdot \tan(\chi)},$$

where the angle $\phi_i = 0, \pi/2, \pi, 3\pi/2$ determines the starting angle of a spiral arm in galactocentric coordinates with respect to the major axis of the bar, and $\chi = 13.8$ deg is the pitch angle of the arms (Ortiz & Lépine (1993)). We use this 4-armed logarithmic spiral in the range between an inner radius of 3.5 kpc and an outer radius of approximately 10 kpc. We do not ensure a smooth transition to the bar in the parametric model. The spiral arms are modelled with a Gaussian profile with FWHM usually ≈ 300 pc, again after Ortiz & Lépine, but we have also computed models with ≈ 500 pc, without improving the fit to the data as described below. In our parametric models we treat this spiral arm model as an enhancement of the density of our standard disc model, keeping all the above spiral arm parameters fixed and varying only the amplitude d_s of the density modulations:

$$\rho_d^{\text{including spiral}} = \rho_d \cdot \prod_{i=1}^4 \left(1 + d_s \cdot e^{-\ln(2) \cdot \Delta r_i^2 / (0.5 \cdot \text{FWHM})^2} \right)$$

where Δr_i is the (approximate) distance to the nearest point on spiral arm i . The projected density is matched to the *COBE/DIRBE* L-band data and the best fit parameters are found with our implementation of the Marquardt-Levenberg algorithm (Press et al. (1994)), now with d_s as an additional fit parameter. These parametric best-fit models (as a function of the bar angle φ_{bar}) are used both as initial models and to define a spiral arm bias term in the penalty function (see below) in the non-parametric deprojection of the *COBE/DIRBE* L-band data.

2.2 The algorithm

Our approach is non-parametric: the idea is to maximize a likelihood function which includes penalty terms encourag-

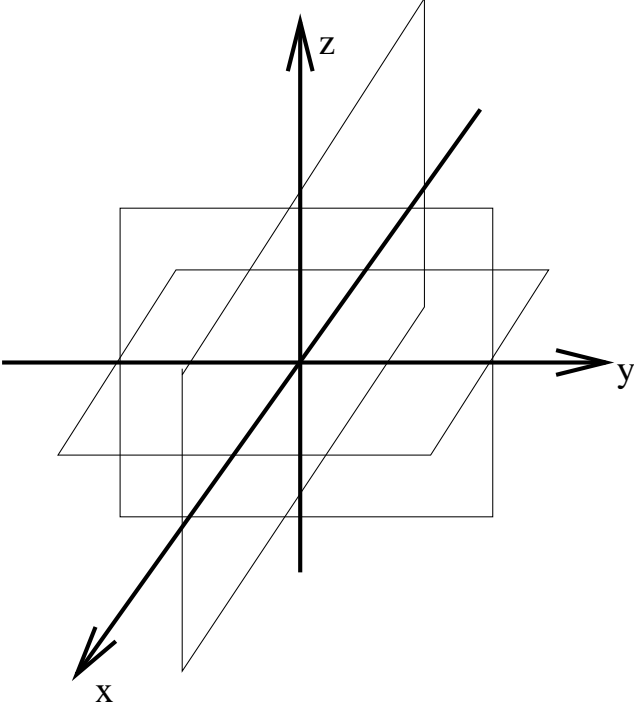


Figure 1. The eight-fold symmetry term in the penalty function encourages symmetry of the density function with respect to the mirror planes shown in this figure. Coordinate directions are in the bar frame.

ing smoothness, eight-fold symmetry and a spiral structure close to the imposed four-armed pattern. Thus also the bar by itself is not forced to obey eight-fold symmetry, but will be nearly triaxially symmetric as far as allowed by the data and the other constraints.

For the technical realization, the model density is defined on a cartesian grid. Stepsizes are identical in x and y . The stepsize in z is smaller than for x and y because we expect the most rapid spatial change of the density along z . The “standard” grid consists of $60 \times 60 \times 41$ points covering a box of $(-5 \text{ kpc} \leq x \leq 5 \text{ kpc}) \times (-5 \text{ kpc} \leq y \leq 5 \text{ kpc}) \times (-1.5 \text{ kpc} \leq z \leq 1.5 \text{ kpc})$ in x, y, z . The size of the box is chosen so as to emphasize the bar region; outside its boundaries the parametric model is left unchanged. This leads to a discontinuity in the density at the grid boundary; for example, averaged over the high-density region $|z| \leq 450 \text{ pc}$ around the grid boundary, the rms discontinuity is $< 1\%$. The likelihood maximisation is done using a conjugate gradient method.

The likelihood function \mathcal{L} maximized by the algorithm is

$$L[\ln(\rho)] = -\left(\frac{1}{2} \cdot \chi_{\text{SB}}^2 + \lambda \cdot D^2[\ln(\rho)] + o \cdot \chi_{\text{s}}^2 + s \cdot \chi_{\text{spiral}}^2\right) \quad (2)$$

where the individual penalty terms are now described in more detail, and λ, o, s are the penalty parameters.

1.Surface brightness term:

$$\chi_{\text{SB}}^2 = \sum_{\text{all SB}(m,n)} [\ln[\mathcal{P}(m,n)] - \text{SB}(m,n)]^2, \quad (3)$$

where $\mathcal{P}(m,n)$ is the projection of the density ρ along

the LOS at the sky position (l_m, b_n) of the corresponding COBE/DIRBE surface brightness data point $\text{SB}(m,n)$ (natural log of flux in MJy/sr). Only the parts of the LOS that are in the model grid are taken into account in the projection. We therefore rescale the observed surface brightness for each LOS by multiplying it with the ratio of the surface density in the box to the total surface density, calculated for the initial parametric model. $\text{SB}(m,n)$ denotes this box-corrected surface brightness. Outliers (data points with a very large distance to the projection of the initial density ρ_0 : $[\ln[\mathcal{P}(m,n)] - \text{SB}(m,n)]^2 \geq 10$) are ignored in the sum eq. (3).

2.Smoothness:

$$D^2[\ln(\rho)] = \sum_{\alpha\beta \in xx,yy,zz,xy,xz,yz} w_{\alpha\beta} \times \sum_{\text{Interior points}(i,j,k)} D_{\alpha\beta}^2[\ln(\rho)] \cdot w_{(i,j,k)}^{\alpha\beta}.$$

This penalty term encourages smoothness of the density distribution by minimizing the total second derivative. All partial second derivatives are taken into account, and are symbolized by their “coordinate direction” $\alpha\beta$. For example $\alpha\beta = xy$ stands for $\frac{\partial^2}{\partial x \partial y}$. All second derivatives are evaluated only at interior grid points not on any boundary of the box. Because the stepsize s_z in the density grid is smaller than the stepsizes $s_x = s_y$, the six “coordinate direction”-terms are given weights $w_{\alpha\beta}$. These are $w_{xx}=w_{yy}=w_{xy}=1$, $w_{xz}=w_{yz}=\left(\frac{s_x}{s_z}\right)^2$ and $w_{zz}=\left(\frac{s_x}{s_z}\right)^4$. The functions $D_{\alpha\beta}$ are first order approximations for the second derivatives along the “coordinate direction” $\alpha\beta$; for example

$$D_{xx} = \ln(\rho_{i+1,j,k}) - 2 \cdot \ln(\rho_{i,j,k}) + \ln(\rho_{i-1,j,k}),$$

$$D_{xy} = [\ln(\rho_{i+1,j+1,k}) - \ln(\rho_{i-1,j+1,k}) - [\ln(\rho_{i+1,j-1,k}) - \ln(\rho_{i-1,j-1,k})].$$

We expect significant differences in the expected second derivatives between different parts of the grid. For example high rates of change of the density are expected at small galactocentric radii. Therefore we give each grid point and “coordinate direction” $\alpha\beta$ additional individual weights $w_{(i,j,k)}^{\alpha\beta}$. We have tried two different approaches for these individual weights. Using the density $\hat{\rho}$ of the initial non-parametric model, we have used

$$w_{(i,j,k)}^{xx} = \ln(\hat{\rho})_{i,j,k} / \frac{1}{4} \cdot [\ln(\hat{\rho})_{i+1,j,k} - \ln(\hat{\rho})_{i-1,j,k}]^2$$

and

$$w_{(i,j,k)}^{xy} = \ln(\hat{\rho})_{i,j,k} / \left[\frac{1}{4} \cdot [\ln(\hat{\rho})_{i+1,j,k} - \ln(\hat{\rho})_{i-1,j,k}] \cdot [\ln(\hat{\rho})_{i,j+1,k} - \ln(\hat{\rho})_{i,j-1,k}] \right].$$

or, in the second approach, $w_{(i,j,k)}^{\alpha\beta} = D_{\alpha\beta}^2[\ln(\hat{\rho})]$. We have found no significant differences between models based the two approaches. Therefore we do not expect a significant influence of the exact definition of these weights on our results.

We have also tried a smoothing term defined on a cylindrical grid, using $\rho(r, \phi, z)$ and a smoothness penalty term

$$D^2[\ln(\rho)] = \sum_{\alpha\beta \in rr, \phi\phi, zz} w_{\alpha\beta} \sum_{\text{Interior points}(i,j,k)} \{ D_{\alpha\beta}^2[\ln(\rho_c)] \cdot G_{\alpha\beta}(r) \cdot w_{(i,j,k)}^{\alpha\beta} \}.$$

Here $G_{\alpha\beta}(r) \equiv 1$ for $\alpha\beta = rr \wedge \alpha\beta = zz$ and $G_{\phi\phi}(r) = r/r_{max}$. In tests comparing the two different smoothing penalty terms we have found that the cartesian smoothing needs somewhat better initial models to give good final results, while the cylindrical smoothing introduces some bias towards round models. However, the main results described in the sections to follow have been checked by doing the calculations with both approaches and were found to be identical. Our results therefore do not depend on the precise smoothing approach and in the following, the cartesian smoothing will generally be used.

To close the discussion of the smoothness penalty term we remark on a technical detail. The algorithm to maximize the likelihood function evaluates the gradient $\frac{\partial \mathcal{L}}{\partial (\ln(\rho_{ijk}))}$. This gradient is modified slightly in the case of a cartesian smoothness penalty term: terms that couple a point to its neighbours of second order (i.e., not their nearest neighbours) are then omitted. We find that without this change the isodensity contours in the outer parts of the final models become rectangular because the cartesian smoothness term favours straight contours parallel to the coordinate axes.

3.Eight-fold symmetry: Triaxial symmetry with respect to three principal planes of the bar (see Fig. 1) is an essential requirement for being able to obtain a three-dimensional luminosity distribution from the *COBE/DIRBE* surface brightness map (Binney & Gerhard (1996)). Bars in external galaxies are observed to be approximately but not strictly eight-fold symmetric (e.g., Sellwood & Wilkinson (1993)); In our deprojection we therefore aim to find a luminosity distribution that is as nearly eight-fold symmetric as is compatible with the data and the smoothness constraint. This is done by discouraging deviations from eight-fold symmetry through the penalty term

$$\chi_8^2 = \sum_{i,j,k} \sum_{\text{pairs}} (\ln(\rho_{i',j',k'}) - \ln(\rho_{i'',j'',k''}))^2.$$

Here the inner sum is taken over all distinct pairs of grid points constructed from the eight mirror-symmetric points of grid point (i, j, k) , that should have identical luminosity density if the distribution were fully eight-fold symmetric.

4.Spiral structure term: Generally there is not enough information in the *COBE/DIRBE* surface brightness data to determine the luminosity distribution in the Galactic spiral arms. Essentially the only information about the spiral arms in these data is an enhanced surface brightness in the arm tangent directions (see also Drimmel & Spergel (2001)). Deriving a sensible model therefore requires using additional, external information on the arm pattern. For most of our models we assume that the Galactic spiral arms in the NIR are described approximately by the four-armed pattern that seems to be most consistent with observations of HII regions, gas, young stars, and NIR starcounts (see Ortiz & Lépine (1993) and the summary in Englmaier & Gerhard (1999)). We leave open the question whether the old population of the Galactic disk follows this four-armed or rather a two-

armed pattern. In practice, we discourage deviations from the disk part of the initial parametric model $\hat{\rho}$ that is also used to start the iterations, which includes the Ortiz-Lépine spiral arm model (Section 2.1). The penalty term is:

$$\chi_{\text{spiral}}^2 = \sum_{k: |z(k)| \leq z_s} \sum_{i,j} [w(k) + \ln(\hat{\rho}_{i,j,k}) - \ln(\rho_{i,j,k})]^2 \quad (4)$$

with

$$w(k) = \ln \left(\frac{\sum_{k, \text{all } i,j} \rho_{i,j,k}}{\sum_{k, \text{all } i,j} \hat{\rho}_{i,j,k}} \right).$$

The outer sum in eq. (4) is computed over all planes parallel to the main plane of the MW with indices k for which $|z(k)| \leq z_s$ with $z_s = 300$ pc, and the inner sum is taken over all points within the current plane. I.e., the model is only biased towards the initial model near the disk plane. The weights $w(k)$ guarantee that the model is encouraged to resemble $\hat{\rho}$ only *in shape*, but not in normalisation. In fact, the normalisation ratios $w(k)$ are usually somewhat different for every iteration step. We have tested that restricting the spiral structure penalty term to $R \geq 3.5$ kpc did not change our models significantly.

2.3 Optimal penalty parameters from test models

Having specified the likelihood function (2), we now need to determine the penalty parameters λ, o, s which set the relative importance of the different penalty function terms. These can be found approximately using known test models by requiring that all terms in the penalty function should be of the same order of magnitude. Otherwise one of the imposed constraints would be given too high or too low weight in the resulting model. Because non-parametric models do differ from the test models employed in this determination, we found it necessary to vary the resulting penalty function parameters within an order of magnitude or so, based on a (subjective) by-eye assessment of the final model.

The special properties of the spiral arm bias term require an additional modification of this simple scheme. The spiral structure is confined to the vicinity of the Galactic plane, and there it is neither very smooth on the scale of a few grid cells nor is it eight-fold symmetric. On the other hand, it penalizes deviations from some model $\hat{\rho}$, which has a similar effect like a regularization term. After some experimentation we found that a good solution is to change the eight-fold symmetry parameter to 20% of its original value in the main plane of the MW and let it linearly rise with distance $|z|$ from the plane to its overall value. Similarly the smoothness penalty parameter is set to only 1 percent of its maximum value in the main plane, but rises very fast $\propto (1 - (1 - |z|/1.5 \text{ kpc})^{10})$ with distance from the central plane.

For part of the problem (data, smoothness, and eight-fold symmetry) we have tested the above choice of penalty parameters with a second approach. We selected two parametric models without spiral structure, that differed by about the same amount that we expect our initial models in deprojections of the *COBE/DIRBE* L-band data to differ from the “true” model. From one of these models we generated artificial data by projecting it onto the sky and

adding Gaussian noise with $\sigma = 0.076^{\text{mag}}$. This is the remaining rms NIR colour variation found by Spergel et al. (1996) for this dereddened *COBE/DIRBE* L-band data set. We then deprojected these data using the second parametric model as initial model and repeated the deprojections for a grid of points in (λ, o) space. For all deprojected models we computed the rms difference between data and projection of the model onto the sky, and the rms difference in the natural logarithm between the “true” model and the deprojected model on the density grid. For computational reasons we could do this only for a coarser density grid. The resulting optimal penalty parameters λ , o , when rescaled to the original grid, agree with the values obtained by the “equal penalty terms” method to within 1-2 orders of magnitude.

2.4 Performance and limitation of the algorithm

We have tested this algorithm with noisy artificial data and initial conditions derived from a variety of test models. Quantitative results will be given in the next section, which studies ambiguities in the deprojection of Galactic bar and disk models from surface brightness data, under the assumptions made. Here we discuss only a few qualitative points.

It is clear that information about the “true” model used to generate the artificial data is increasingly hard to recover as the noise level approaches the magnitude of the signal that differentiates between different models on the sky. On the other hand, we have found that some noise is helpful as a “catalyst” to induce changes in the model.

The initial models given to the algorithm differed from the “true” model by various amounts. We find that the initial model must not be too far from the “true” model. This is hard to quantify by a distance criterion. However, the effects that occur if the initial model is not suitable are easily visible in cuts through the density grid, and it is therefore possible to reject such models.

If the initial model is suitable, convergence to a luminosity distribution that fits the surface brightness map under the assumed smoothness, symmetry and spiral structure constraints typically takes 20-30 iterations. Otherwise the progress of the iterations becomes very slow at some point and the model may be caught near something like a secondary minimum. In such cases, an iteration step that would be required to improve the surface brightness fit is often not undertaken because it would move the model too far away from eight-fold symmetry. Some secondary minima of the likelihood function correspond to nearly perfectly eight-fold symmetric models which have, however, physically unreasonable density distributions. The probability that the algorithm ends up with such a model increases with the distance between the initial model and the “true” model.

Introducing a smoothness term in a complicated χ^2 fitting problem often lessens the importance of such secondary minima. Here the additional problem is that a third constraint, eight-fold symmetry, must be introduced to restrict the range of possible solutions (for fixed bar angle, the requirement of eight-fold symmetry restricts the solution to a small subset of the very large set of luminosity distributions which all project to the same surface brightness distribution, Binney & Gerhard (1996)). It is easy to see then that

secondary minima based on a balance between data and symmetry terms can appear in spite of the smoothing.

If the requirement of eight-fold symmetry is imposed only weakly, a characteristic artifact appears in many models which we have termed *Finger-to-Sun* (FTS) effect. This consists of excess luminosity features in the nearby disk pointing towards the observer. These arise because the deprojection algorithm preferentially changes grid cells near the observer. The reason for this is that grid cells near the observer appear larger on the sky, and therefore contribute to many more surface brightness pixels than distant grid cells do. Consequently, for a model that is off from the “true” model underlying the data by a fixed fraction of the density in all grid cells, the total gradient $\partial\chi_{\text{SB}}^2/\partial(\ln\rho_{ijk})$ is much larger for grid cells near the observer (the actual value contributed to the surface brightness of a given pixel is independent of the line-of-sight distance of the contributing grid cells). Therefore, without smoothing and symmetry penalty terms, the luminosity model would be changed mainly near the observer, resulting in the described FTS effects.

3 HOW WELL-DETERMINED IS THE DEPROJECTION OF THE BAR?

As a test application of our algorithm, we investigate in this section possible degeneracies in the deprojection of a bar model for fixed bar angle, keeping $\varphi_{\text{bar}} = 20$ deg throughout this section. More precisely, we ask what is the range of bar luminosity distributions that is compatible with given surface brightness data similar in quality to the *COBE* data which we will use in §5 for investigating the luminosity structure of the inner Galaxy. We find that there exists a sequence of parametric models with different bar elongations in the Galactic plane and correspondingly different density concentrations, that look very similar on the sky. Then we use the non-parametric algorithm to estimate the width of the “valley” of acceptable models around the sequence of degenerate parametric models. Finally, we show that observations such as the apparent magnitude distributions of clump giant stars by Stanek et al. (1997) contain sufficient distance information to break this degeneracy, which incidentally is different from the well-known degeneracy in the bar angle φ_{bar} (Binney, Gerhard & Spergel (1997), Zhao (2000)).

We first generate artificial data by projecting a parametric model onto the sky. This model (denoted slp) is defined by eq. (1), with bar parameters $\eta = 0.5, \zeta = 0.6, a_m = 1.8$ and disk parameters $z_0 = 208$ pc, $R_d = 2.44$ kpc, and does not have spiral arms. We add Gaussian noise to these data, similar in amplitude to that expected for the *COBE/DIRBE* L-band data used later, for which $\sigma_{\text{SB}} = 0.076^m$ (Spergel et al. (1996), see Section 4.1 for a discussion). The parametric model is a best-fit model for the *COBE/DIRBE* L-band data for $\varphi_{\text{bar}} = 20$ deg.

Next we fit other parametric models to these model surface brightness data. In these models we hold fixed the bar elongation η . To decide whether a model is a valid match to the data, we define two criteria: (i) The average square deviations of the projected model from the artificial data in magnitudes (hereafter model RMS) must not be worse by more than 20% in the bar region $|l| < 36$ deg \wedge $|b| < 11$ deg than for the “true” model. (ii) There must not be major

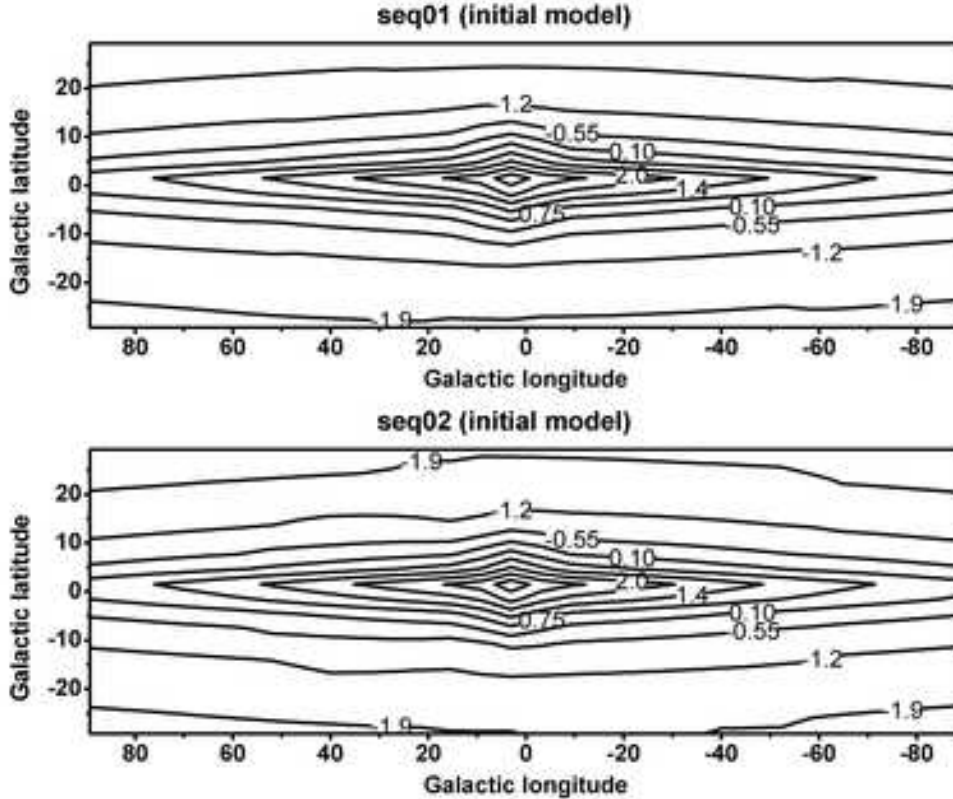


Figure 2. Two parametric models on the degenerate sequence for $\varphi_{\text{bar}} = 20$ deg. Note how similar models s1p (upper panel) and s2p (lower panel) appear to the observer.

parts of this region where a systematic error larger than the approximate average statistical error occurs in the residual map.

With these criteria, we find a sequence of parametric models that are indistinguishable on the sky, i.e., for which systematic deviations between model and data are smaller than the noise in the data. Figure 2 compares model s1p with another parametric model s2p, which is on this sequence. Model s2p has bar parameters $\eta = 0.603$, $\zeta = 0.68$, $a_m = 1.5$ kpc, significantly different from model s1p, but looks very similar on the sky. Models on this sequence are characterized by a degeneracy between the input bar elongation in the xy -plane, η (see eq. 1), and the central concentration of the model. This is parametrized as the half mass radius $r_{0.5}$, defined as the elliptical radius $r_{0.5} = \sqrt{x^2 + \frac{y^2}{\eta^2} + \frac{z^2}{\zeta^2}}$ which contains half of the mass of the bar/bulge inside an elliptical radius of 3.5 kpc.

In Fig. 3 the sequence of parametric models is depicted in the $r_{0.5} - \eta$ plane as the filled hexagons connected by the full line. The parametric model at the lower-right end of this sequence is just still a valid model as defined above. For models with even smaller η the deviations from the artificial data rise rapidly. Fig. 4 shows the model RMS on the sky, for parametric models both on the sequence and on its extensions to higher and lower η , where the latter fail to pass our criterion for a valid model. On the high- η extension of the sequence, the model RMS rises fairly slowly, but these models have regions with too large systematic deviations from the projected data, which increase with increasing η . From

Fig. 3 parametric models thus have an uncertainty in their model parameters of ± 0.1 in η and $\pm 20\%$ in $r_{0.5}$ for given data on the sky.

We now consider non-parametric models obtained with the deprojection algorithm described in §2. First, we start the algorithm from initial models on the parametric sequence, resulting in models s1 and s2 from the initial s1p and s2p. For the non-parametric models we estimate η by measuring the elongations of the surface density contours of the bar, determined from a projection of the model density along the z -axis, but excluding the region $|z| \leq 225$ pc to reduce the impact of the strong axisymmetric disk. This is a good approximation because the bulges in these models are near-ellipsoidal. We measure the half-mass radius $r_{0.5}$ from the density distribution of the bar/bulge only, obtained by subtracting the disk density of the parametric initial model given to the algorithm, from the density distribution of the final non-parametric model. We have checked by visual inspection that the resulting bulge densities are reasonable. Fig. 3 shows that models s1p and s2p lie very close to s1 and s2. The similarity of initial and final models is also obvious from a comparison of cuts through the densities. We conclude from this exercise that the deprojection algorithm does not introduce any significant bias in the final model, e.g., in the resulting value of η .

We will next discuss non-parametric models started from parametric models off the degenerate sequence, in order to investigate how broad the valley of acceptable models surrounding the sequence is. Several such models (s3-s10)

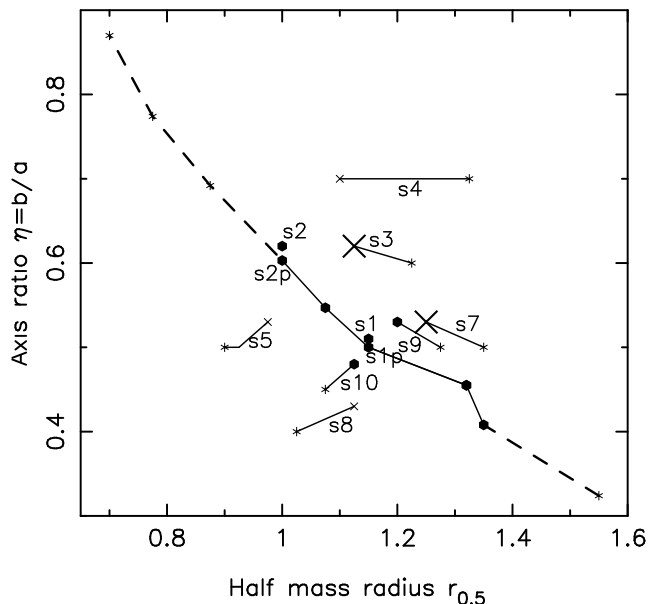


Figure 3. Parametric and non-parametric luminosity models for surface brightness data obtained from projecting model s1p under $\varphi_{\text{bar}} = 20$ deg and adding noise. All models are plotted in a plane according to their half-mass radius $r_{0.5}$ and bar elongation η . The full line delineates the sequence of degenerate parametric models which project to indistinguishable SB data. These models are indicated by the filled hexagons along this line. The dashed lines connect parametric models (stars) on the extensions of this sequence towards high and low η . These models are not acceptable, because they either show too large systematic deviations from the data, or have quality grade $F > 3$ (see eq. 5). Models s1-s10 are obtained from non-parametric, iterative deprojections of the model SB data. Of these, s1,s2 were started from parametric models (s1p, s2p) along the sequence. Their proximity to the original (s1p, s2p) demonstrates the absence of significant bias in the algorithm. The other non-parametric models were started off the sequence (stars on one end of the short lines denote the initial configurations) and are separated in the figure into acceptable final models (filled hexagons, $F \leq 3$), marginally acceptable models ($3 < F \leq 4$, large “X”), and unacceptable models ($F > 4$, small “x”).

are shown in the $r_{0.5} - \eta$ -plane of Fig. 3, as stars for the respective initial parametric models, and as hexagons and crosses for the final non-parametric density distributions after around 50 iterations. Clearly the algorithm evolves these models to the vicinity of the parametric sequence. Whether these non-parametric models are acceptable cannot be decided only on the basis of the model RMS on the sky, however. For in a non-parametric model, substantial grid cell to grid cell noise can be introduced in order to improve the match to the data, which beyond a certain point is clearly unphysical. Therefore some measure of smoothness must be introduced in judging a model’s validity.

We measure the smoothness S of some model M as the sum of the absolute differences in logarithmic density, between M and a smoothed version of M . S will be small for smooth M and large for noisy M . In determining S we sum only over grid cells with $|z| \leq 750$ pc, to avoid contributions from fluctuations in regions of the density grid where the density is very small. We smooth a model as follows, working with logarithmic model densities: (i) We resample

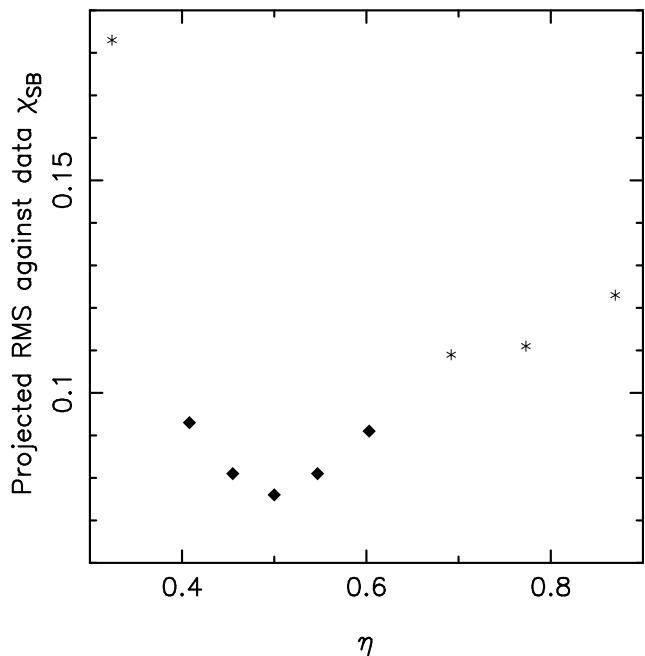


Figure 4. RMS SB residuals, χ_{SB} , in magnitudes, for parametric models on the degenerate sequence, plotted as a function of in-plane axial ratio η (equivalent to varying $r_{0.5}$). Diamonds indicate models on the sequence, stars models on the extensions of the sequence.

each z -plane of the model on a cylindrical grid of 30 linearly spaced points in $r = \sqrt{x^2 + y^2}$ out to $r = 7$ kpc, and 60 points in azimuth ϕ . (ii) We smooth the model over 5 points, first in the ϕ -coordinate, then in r , and finally in z , using second order polynomials (Savitzky-Golay filters, see Press et al. (1994)). In this way azimuthal gradients in the central parts of the model are not smoothed away. (iii) We re-interpolate to the original cartesian grid. (iv) In models with spiral arms, this procedure must be modified because the spiral arms imply density changes on small scales. For example, on a circle at galactocentric radius 5 kpc, the distance between adjacent points in ϕ in our smoothing algorithm is ≈ 500 pc; therefore the smoothing length is of the same order as the spiral arm FWHM. Thus before actually smoothing the model, we subtract from the density at every grid point the density of the spiral arm contribution in the initial parametric model, rescaled in each xy -plane separately. The rescaling factor for each xy -plane is determined by requiring that in this plane the rescaled mass of the initial model is the same as that of the (non-parametric) model that we actually smooth. Having subtracted the rescaled spiral model, we smooth the remaining luminosity distribution as in (ii), and then add the subtracted spiral density back to the smoothed density. This spiral arm preservation procedure is restricted to model planes with $|z| \leq 450$ pc, because the initial spiral models only extend to this height. The procedure ensures that the spiral arm component does not contribute to the final difference between M and the smoothed version of M , i.e., to S .

Figure 5 shows the final non-parametric models considered in this section in a plane of model RMS χ_{SB} and smoothness S . The best non-parametric models have $S \simeq 4000$, parametric models have typically $S \simeq 3000$, and mod-

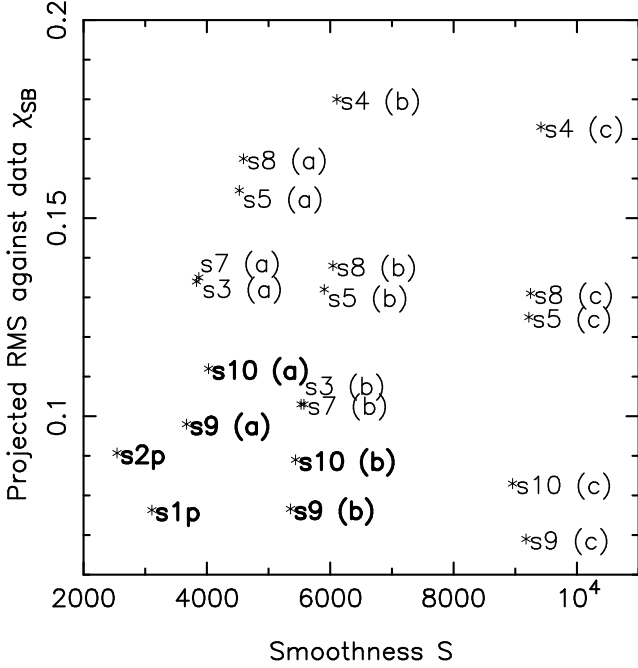


Figure 5. Non-parametric luminosity models s3-s10 obtained from model SB data with the algorithm described in Section 2. The parametric models s1p from which the data were generated, and s2p on the degenerate sequence, are also shown. The models are characterized by their smoothness S (smaller S means smoother), and by their rms difference χ_{SB} with respect to the SB data on the sky, in magnitudes. Most models have been calculated with three values of the parameter λ ; the last symbol “a”, “b” or “c” in the non-parametric model name (for example s4a) indicates λ , decreasing from “a” to “c” in multiplicative steps of 10. Model names printed in bold denote acceptable models, i.e., have quality grade $F \leq 3$ (see eq. 5).

els with $S \gtrsim 7000$ are not smooth enough to be acceptable. We illustrate this in Figure 6, which shows cuts through model s4c (which has $S \approx 9400$) at $z = 75$ pc and model s10b (with $S \approx 5400$), also at $z = 75$ pc.

We can now define a criterion to decide whether a non-parametric model is an acceptable representation of the SB data. To this end we introduce the quality grade

$$F = \left(\frac{\chi_{SB}}{0.076^m} \right)^2 + \left(\frac{S}{S_0} \right)^2, \quad (5)$$

where S_0 is a measure of S for the “best” non-parametric models we find. We use the average $S_0 = 4827$ of the three non-parametric models s9(a), s9(b), s10(a) printed in bold on Fig. 5. F is smaller for models that fit the data better and that are smoother. The maximum value of F for an acceptable model is somewhat subjective; we decided for $F \leq 3$. This results in $\chi_{SB} \lesssim 0.11^m$ for a model with $S \sim S_0$ and $S \lesssim 6800$ for a model with $\chi_{SB} \sim 0.076^m$. Models which violate the last criterion are not smooth enough to be viable (see Figure 6).

We have used the F -criterion to separate the final non-parametric models s3-s10 in Fig. 3 into valid and non-valid models. Filled hexagons indicate acceptable models ($F \leq 3$), large “X” marginally acceptable models with $3 < F \leq 4$, and small “x” unacceptable models with $F > 4$ (of the three models computed with different λ , that with lowest F is

always shown). The hexagons thus mark the width of the valley of acceptable models associated with the sequence. This width, set by the model RMS and smoothness, translates to an uncertainty in the structural parameters of a non-parametric model of $\approx \pm 0.1$ kpc in the half-mass radius $r_{0.5}$ and $\approx \pm 0.05$ in the bar elongation η . These are smaller than the uncertainties due to the existence of the degenerate sequence itself.

Having quantified the uncertainties due to the extent and width of the degenerate sequence, we now show that these uncertainties can be much reduced if additional distance information is used, such as is available in the apparent magnitude distributions of clump giant stars. Stanek et al. ((1994), (1997)) have observed clump giant distributions in a number of fields towards the bulge. In Fig. 7 we plot such distributions for three models on the parametric sequence and one at the edge of the valley of acceptable models around it. The relevant quantity is ρr^3 , which has one extra power of r over that from the volume effect, due to the conversion of distance to magnitudes. The predicted distributions are different for the models on the sequence. Depending on the errors in the observations, it is thus possible to discriminate between these models through their clump giant distributions. The clump giant distributions of models s3p and s1p are very similar; however, these models can be discriminated on the basis of their projected surface brightness maps, using e.g., the F -criterion. Model s3p is not an acceptable model for the data generated from s1p. The experiments conducted in this section make it likely that using the goodness-of-fit F and the clump giant constraints together breaks the degeneracy in bar/bulge models that exists for fixed φ_{bar} .

4 DEPROJECTION OF THE INNER GALAXY

In this section we apply the algorithm to the *COBE/DIRBE* data, using the dust-corrected L-band map of Spergel, Malhotra & Blitz (1996). These authors took the $240\mu m$ *COBE/DIRBE* map as a tracer for the distribution of dust to correct the *COBE/DIRBE* near infrared (NIR) J,K,L and M-band data for dust absorption. They simultaneously fitted parametric models for the dust and stars and with these models computed dereddened NIR surface brightness maps. The K-band emission near $\lambda \approx 2.2\mu m$ is dominated by starlight and only moderately affected by dust. In the L-band, near $\lambda \approx 3.5\mu m$, emission by hot dust and interstellar gas may be slightly more important, but dust extinction is reduced by about a factor of two in magnitudes as compared to the K-band. Because in some inner Galaxy regions extinction is significant even in the K-band, we have decided to use the L-band data in this paper.

After dereddening Spergel et al. (1996) found a mean dispersion $\sigma \approx 0.076^m$ in colour between the K- and L-band maps. If we could assume identical Gaussian noise in both maps, $0.076^m/\sqrt{2}$ would be a straightforward value to use for the SB error in the L-band, σ_{SB} . However, the dominant sources of noise are probably systematic errors in the dust correction, correlated over several pixels and between the NIR maps, especially near the galactic equator. In this case the true errors in the data would be larger. We therefore take a more conservative approach and use $\sigma_{SB} \approx 0.076^m$. In

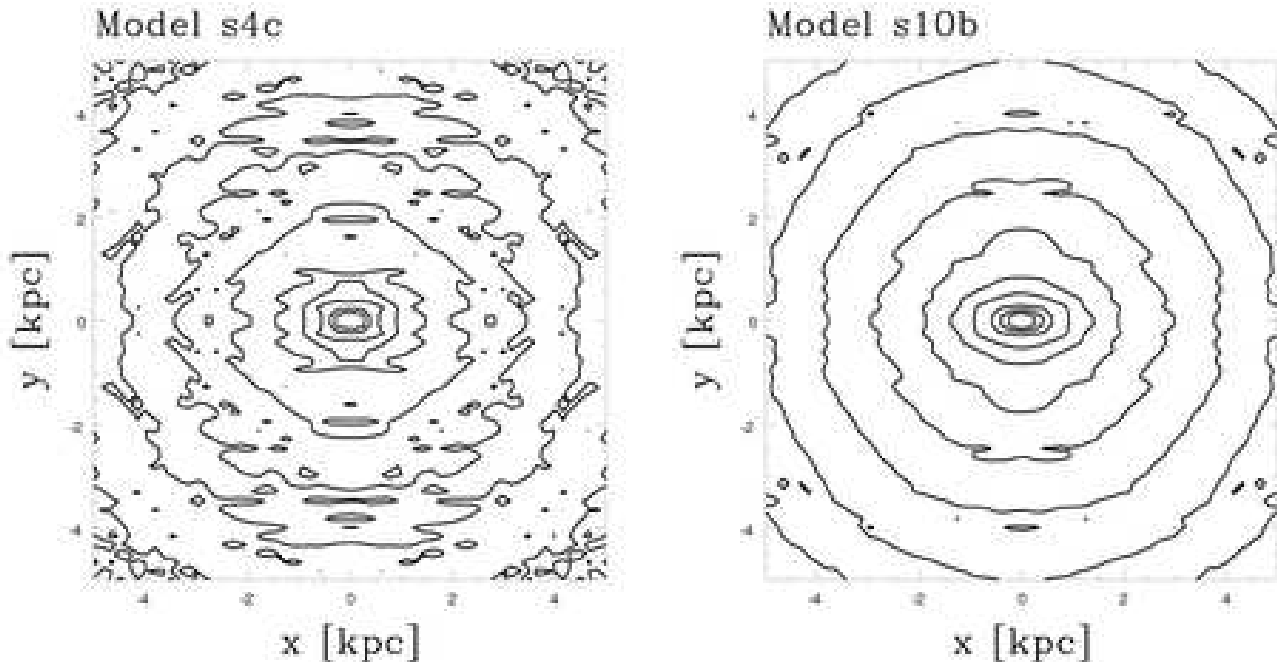


Figure 6. A comparison of cuts through two models with significantly different smoothness S at $z=75$ pc. Left: Model s4c ($S \approx 9400$) Right: Model s10b (with $S \approx 5400$). We consider model s4c not smooth enough to be acceptable.

the non-parametric deprojections of the NIR data described below we have therefore tailored the smoothness penalty function parameters such that we get models with RMS of this order.

The models that we obtain from deprojecting the *COBE/DIRBE* L-band data will then be verified a posteriori by comparing with the apparent magnitude distributions for clump giant stars, measured by Stanek et al. ((1994), (1997)) along certain lines-of-sight towards the Galactic bulge. Clump giants have nearly identical absolute magnitudes with a small dispersion of $\sim 0.2\text{--}0.3^m$, and it is therefore possible to derive their distance distribution (in a statistical sense) from their observed magnitude distribution. Stanek et al. (1997) analysed colour magnitude diagrams (CMDs) in several OGLE fields, including Baade’s window and two nearly symmetric fields at $(l, b) \approx (-4.9 \text{ deg}, -3.4 \text{ deg})$ and $(5.5 \text{ deg}, -3.4 \text{ deg})$. They determined extinction-insensitive magnitudes $V_{V-I} = V - 2.6 \cdot (V - I)$, and plotted histograms of the number of stars as a function of magnitude using $\Delta V_{V-I} = 0.05^m$ -bins for the stars in the part of the CMD dominated by bulge red clump stars. The red clump distributions along these LOS peak at different distances; using a bootstrap technique Stanek et al. (1994) determined a relative distance modulus of 0.37 ± 0.025^m between the LOS at $l \approx 5 \text{ deg}$ and $l \approx -5 \text{ deg}$, and 0.15 ± 0.02^m between Baade’s window and the field at $l = -4.9 \text{ deg}$. These asymmetries provide independent evidence for a non-axisymmetric luminosity distribution in the inner few kpc of the MW, but will be used here to check the three-dimensional luminosity distribution of our models for the L-band flux data.

In §4.1 and §4.2 we deproject the data with and without inclusion of spiral structure in the model, using a bar angle $\varphi_{\text{bar}} = 20 \text{ deg}$ in both cases. This will demonstrate that inclusion of spiral structure leads to a better model for the

COBE/DIRBE L-band data and results in a more elongated shape for the barred bulge. In §4.3 we constrain the acceptable range of bar angle from a set of models with different φ_{bar} together with the clump giant data.

In all cases, the non-parametric density estimation procedure begins with fitting a parametric model to the data. This is used in the non-parametric deprojection in three ways: (i) As starting model of the iterations, (ii) to correct for the limited size of the model density grid and (iii) in models that include spiral structure, to define the spiral structure penalty function term.

4.1 Models with bar but without spiral arms

To find a model for the *COBE/DIRBE* L-band data without spiral arms, we start the iterations from the parametric model given by Binney, Gerhard & Spergel (1997), and set the spiral structure penalty term in the likelihood function to zero. Fig. 8 shows the surface brightness map of this non-parametric model compared with the *COBE/DIRBE* L-band data. It fits the *COBE* data well; the iterations were stopped when the RMS of the model reached 0.073^m . On the left side of Fig. 9 we show two cuts through this model, in the upper panel a cut in the xy -(main) plane, and in the lower panel a cut parallel to the xz -plane, at $y \approx 85 \text{ pc}$. In the xy map we can see overdensities that point from the observer (at $x \approx 7.5 \text{ kpc}$ and $y \approx 2.7 \text{ kpc}$) towards the tangential points of the spiral arms, at approximately $l = \pm 30 \text{ deg}$ and $l = -50 \text{ deg}$ (see also Drimmel & Spergel (2001)).

Can we find a model of the MW without spiral arms which fits the *COBE/DIRBE* L-band data as well as this model, and does not have such features? To try to eliminate these overdensities, we have computed models with larger penalty parameters for deviations from eight-fold symmetry

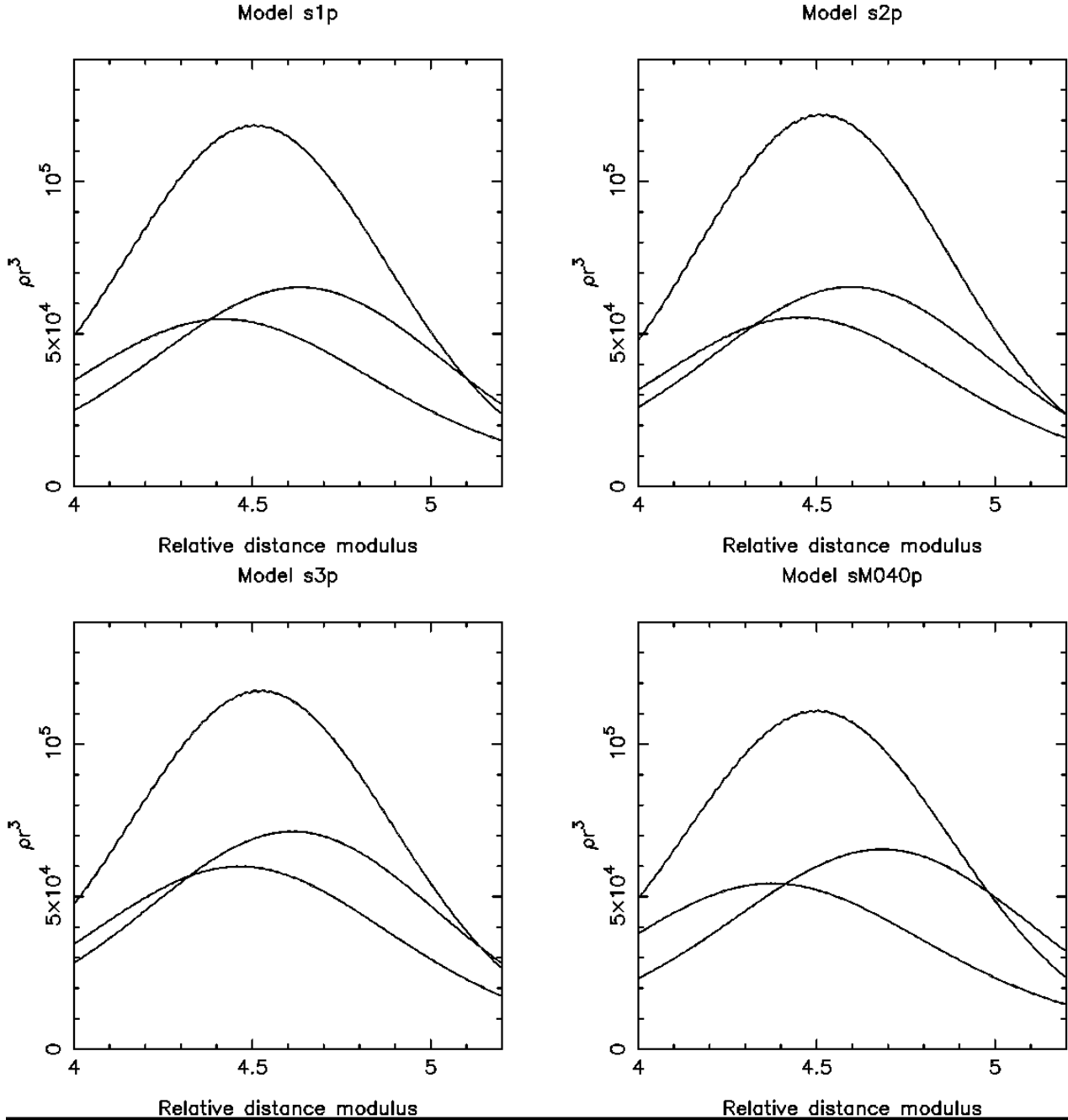


Figure 7. Predicted number of clump giant stars in three fields observed by Stanek et al. (1997), versus relative distance modulus in magnitudes, for parametric models s1p (upper left), s2p (upper right), s3p (lower left), and the parametric model with bar elongation 0.41 also along the degenerate sequence in Fig. 3 (lower right). From the differences in height and location of the peaks in these distributions, it is possible to discriminate between models on the sequence. However, a comparison of the two panels on the left shows that some models off the sequence can mimic the clump giant distributions of models on the sequence. Such models have to be discriminated by their goodness-of-fit for the surface brightness data.

and/or smoothness. However, we have only found models which either contain similar features in the directions to the spiral arm tangent points and achieve a “good” model RMS $\approx 0.07^m$, or models which are smooth and nearly eight-fold symmetric without such features, but which then fit the data badly (model RMS $\gtrsim 0.2^m$). Smooth models which fit the data well without these features do not seem to exist. This suggests that a spiral arm component is implied by the data.

I.e., the luminosity in these features is real, but the shift towards the observer is due to the FTS effect discussed in §2.4.

We mention that a similar effect was observed by Binney, Gerhard & Spergel (1997) in their Richardson-Lucy (RL) models. They used the same data of Spergel et al., and in their models found symmetric density enhancements at 2–3 kpc down the minor axis of the bar. They suggested

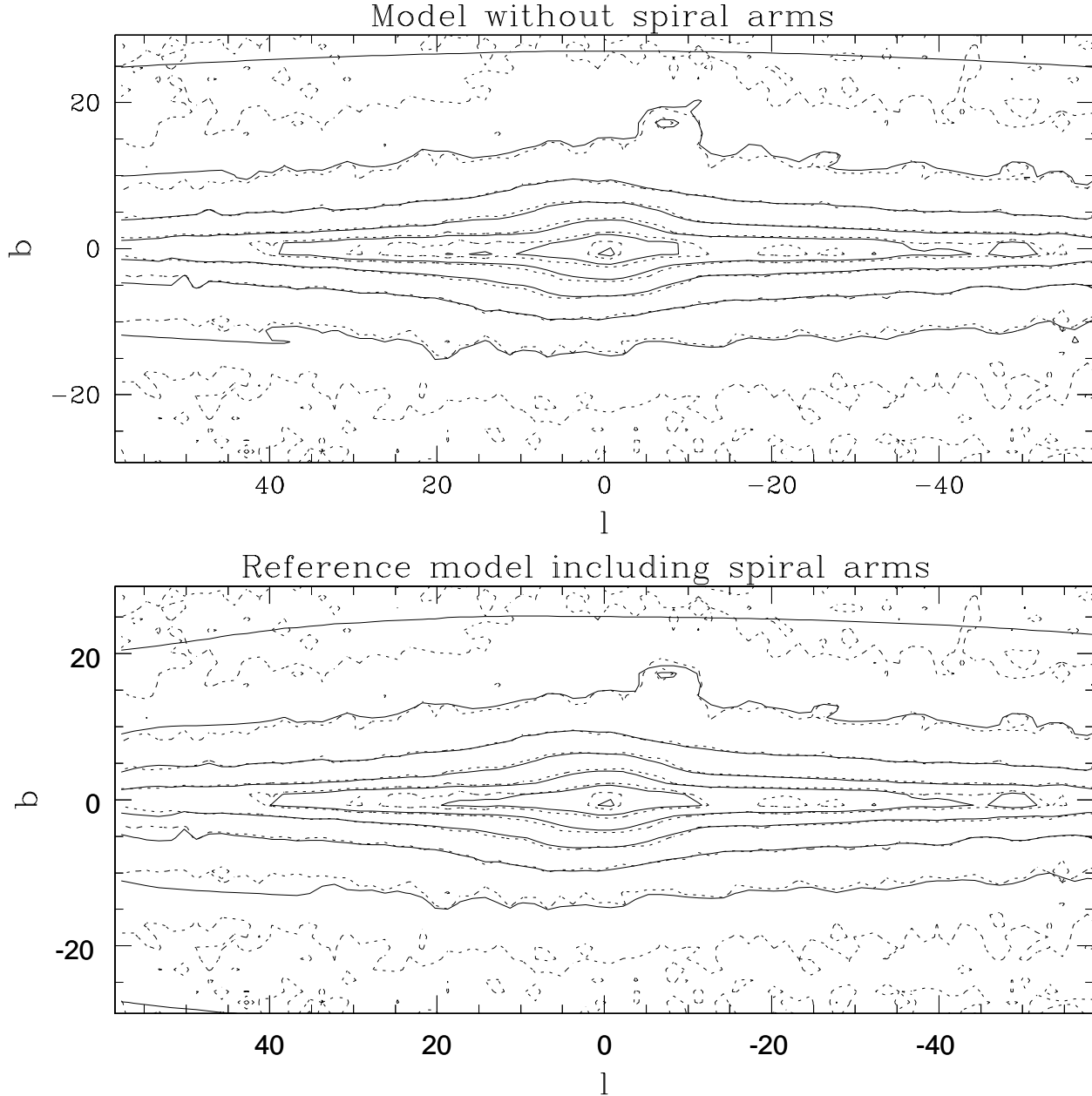


Figure 8. Surface brightness maps of the model without spiral arms (upper panel), and our reference model 20A including spiral arms (lower panel). Full contours show the model surface brightness, dashed contours the *COBE/DIRBE* L-band data. Contour levels are in magnitudes with some arbitrary offset, common to both panels. Both surface brightness maps are very similar and fit the *COBE/DIRBE* L-band data with very similar χ^2 . The underlying models are non-parametric on a grid of $5 \times 5 \times 1.5 \text{ kpc}^3$ and are continued by the initial parametric models outside of this grid for the projection onto the sky.

that these features might be caused by spiral arms being symmetrized by the RL algorithm, which forces the models to be eight-fold symmetric. In contrast to the RL models our deprojection algorithm favours changes to the model density near the observer, and so in the model discussed here the spiral arm overdensities are placed near the observer. The projected bar elongation in our model without spiral arms is 0.56 ($|z| > 225 \text{ pc}$), comparable to that in the model of Binney, Gerhard & Spergel (1997).

4.2 Models with bar and spiral arms

We have seen that models for the MW L-band luminosity density develop overdensities near the observer, towards the tangential directions of Galactic spiral arms, when started from triaxially symmetric initial distributions. Thus we now proceed with a non-parametric density estimation of the data by a model which includes spiral arms. We show that the inclusion of spiral structure not only improves the model

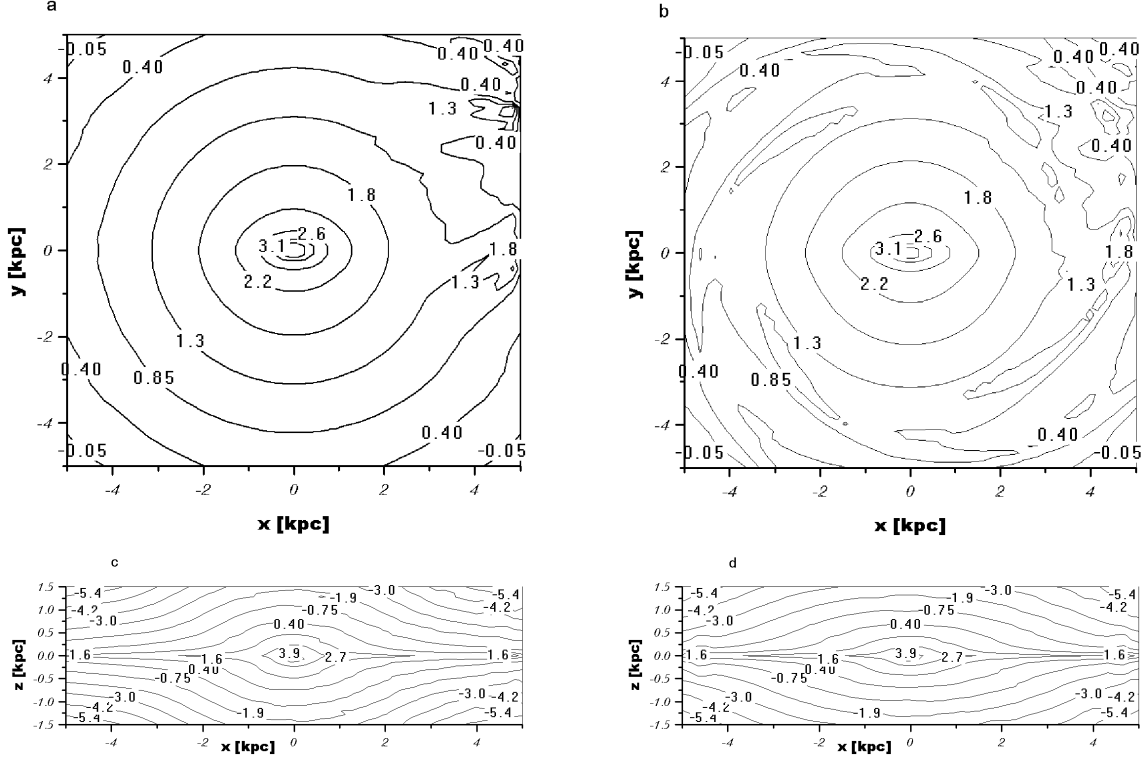


Figure 9. Comparison of the models with and without spiral structure: in the main plane of the MW (upper panels), and in a plane parallel to the major and minor axes of the bar at the first grid point $y \approx 85$ pc (lower panels). Both models are for bar angle 20 deg. Contours are in logarithmic density (in CLU/kpc^3), and printed in the plot. Left: The model without spiral structure, obtained from a (parametric) triaxially symmetric initial bar model. This model shows deviations from eight-fold symmetry in the xy -map. These overdensities approximately point from the observer (at $x \approx 7.5$ kpc and $y \approx 2.7$ kpc) towards the tangential points of the spiral arms. Right: Our reference model 20A including spiral arms. Both the (parametric) initial model and the penalty function in this non-parametric density estimation contain a spiral structure term.

for the *COBE/DIRBE* L-band data, but also results in a better match to the LOS distributions of clump giants towards certain bulge fields. We also show that the derived structure of the bulge/bar does not depend significantly on whether the assumed spiral model is two or four-armed.

First we fit a parametric model to the *COBE/DIRBE* L-band data, continuing to assume a bar angle $\varphi_{\text{bar}} = 20$ deg. This model has the following bulge parameters (see §2.1): $\eta = 0.31$, $\zeta = 0.38$, $a_m = 2.8$ kpc, $a_0 = 0.1$ kpc, $\rho_b^0 = 1180$ CLU, bar angle $\varphi_{\text{bar}} = 20$ deg; disk parameters: $R_d = 2.2$ kpc, $\alpha = 0.65$, $z_0 = 0.19$ kpc, $z_1 = 0.042$ kpc, $\rho_d^0 = 0.54$ CLU/ kpc^3 ; and spiral arm amplitude: $d_s = 0.90$, for the four-armed logarithmic spiral arm model similar to that of Ortiz & Lépine (1993). Here CLU are *COBE* luminosity units as in Binney et al. (1997).

Starting the algorithm from this configuration and including the spiral structure penalty term, we find a best non-parametric density model. This model was selected from a number of calculations run to fine-tune the penalty function parameters, optimizing both the RMS and the model smoothness. This model, stopped at $RMS \approx 0.079^m$, is one of our best if not the best model, and will be used as reference model “20A” in what follows, deferring the discussion of the acceptable range of φ_{bar} to Section 4.3 below. The RMS for this model is similar to that for the model without spiral arms; the difference is not significant. Correspond-

ingly, both models look very similar on the sky and match the data well; see Figure 8. The main difference is in the three-dimensional structure: Figure 9 shows cuts through both models. In the model with spiral arms, these arms provide most of the non-axisymmetric density. Some residual luminosity is still required towards some of the arm tangent points, but deviations from point-symmetry in the Galactic plane near the Sun ($x \geq 3$ kpc, $|y| \leq 5$ kpc) are reduced by a factor of $\simeq 4.5$ (NB: the spiral arms remain nearly point-symmetric during the iterations).

The quality of the model fit to the *COBE/DIRBE* L-band data, especially for the non-axisymmetric bar/bulge, is visualized by the asymmetry maps shown in Figure 10. These maps show the difference between the logarithmic fluxes at positive and negative longitudes, $SB(|l|, b) - SB(-|l|, b)$ for both our reference model 20A and the *COBE/DIRBE* L-band data. Generally, the model is smoother than the data, but it reproduces the main bar-related features of the observed map well. Note the good recovery of the regions with clear bar signature around $(l, b) \approx (8 \text{ deg}, \pm 5 \text{ deg})$, and the change of sign of the asymmetry near the galactic centre. Here the far side of the bar appears brighter, a signature of a bar with its near end at positive longitudes (Blitz & Spergel (1991)). The most obvious differences between both maps are in a strong feature at $(l, b) \approx (14 \text{ deg}, 0 \text{ deg})$ in the observed map, which may

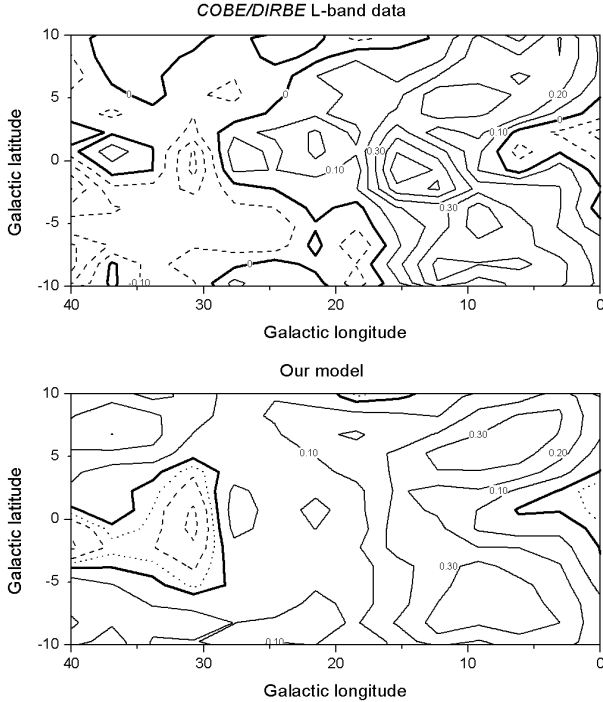


Figure 10. Asymmetry maps for the *COBE/DIRBE* L-band data and for the reference spiral model. The *COBE* data were smoothed with a Savitzky-Golay filter (Press et al. 1994, setting their $M = 5$) to reduce noise. Contours show the asymmetry in magnitudes between positive and negative longitudes. Dashed contours indicate negative values. Positive values indicate that the MW is brighter at positive longitudes. Contour spacing is 0.1^m , and the bold contour is at 0^m (no left-right asymmetry). In the plot for the model a dotted contour is drawn additionally at -0.05^m .

be local, and in the contours near zero asymmetry, which are most affected by noise.

Figure 11 shows the density of model 20A projected along the z -axis for $|z| > 225$ pc. The density near the main plane of the MW is excluded to avoid modifying the bar contours by the strong, nearly axially symmetric inner disk component. In model 20A the bar is more elongated than in the model without spiral arms. This is because for the relative geometry of the arms, the bar, and the position of the Sun, the spiral arms make the model appear broader in longitude on the sky, and for fixed observed asymmetry this allows the bar to be more elongated in the plane. The projection also stresses the true extent of the bar, which is $\simeq 3.5$ kpc. The measured projected bar elongation in the xy -plane is $\simeq 10:3-4$. The contrast in the total face-on surface density between $(x, y) = (2.5 \text{ kpc}, 0)$ and $(x, y) = (0, 2.5 \text{ kpc})$ is a factor of $\simeq 1.6$. A fit to the disk profile in the radial range between 3.5 kpc and 5.5 kpc gives an exponential radial scale-length of 2.1 kpc.

We now compare the three-dimensional structure of the model to the observations of Stanek et al. ((1994), (1997)). These authors determined the line-of-sight distributions of clump giant stars for a number of fields towards the bulge/bar. Because these stars are of nearly identical absolute magnitude within a small dispersion, measuring their brightness distribution at a certain position on the sky pro-

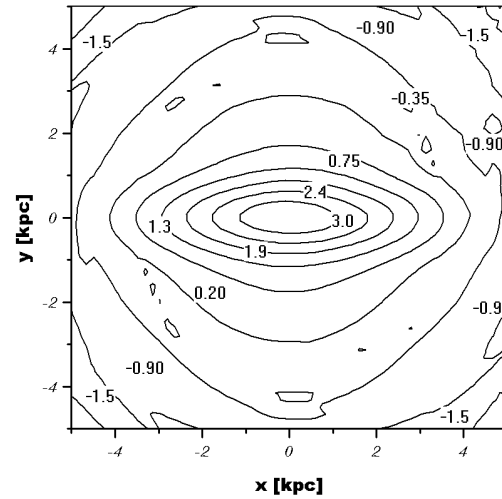


Figure 11. Projection of our model 20A onto the xy -plane. To avoid modifying the bar contours by the strong, nearly axially symmetric disk component, only the density at $|z| > 225$ pc was integrated. The length of the bar is $\simeq 3.5$ kpc and its elongation is $\simeq 10:3-4$. Contours are in logarithmic surface density, with relative contour values indicated on the plot.

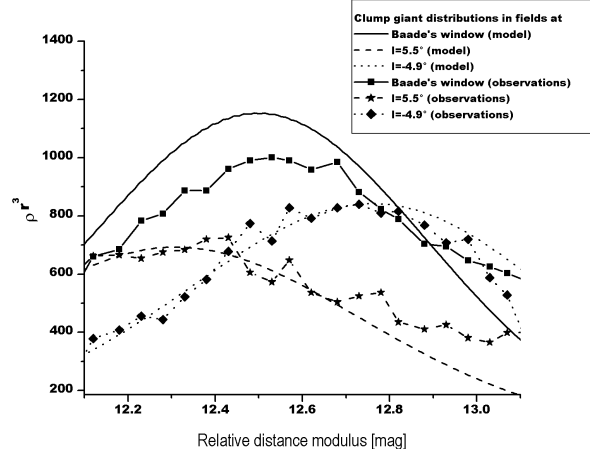


Figure 12. Line-of-sight distributions of clump giants in the directions of three fields observed by Stanek et al. (1994, 1997), with symbols as given in the figure legend. The abscissa is their V_{V-I} . For field M7 the observed counts were averaged over two CCD frames of equal angular size; for field M5 one CCD frame and for Baade's window six frames were used. The curves show our best-fit model including spiral arms. For the model, two constants were adjusted by eye as follows: (i) The model distributions were shifted along the abscissa such that the $l = 5.5$ deg and $l = -4.9$ deg peaks match best the locations of the observed peaks. (ii) The normalisation of the model curves was determined such as to approximately match the normalisation of the observed distributions in the fields M5 ($l \approx -4.9$ deg) and M7 ($l \approx 5.5$ deg). The resulting shift and normalisation are then applied to all model distributions simultaneously. All model distributions are convolved with an assumed width of the clump giant intrinsic luminosity distribution of 0.3^m .

vides a profile of their density along the respective LOS. The apparent magnitude of the peak of the distribution locates the highest-density point along the LOS. The difference in the apparent magnitude of the peak between various bulge fields, especially between the fields at $l \approx 5.5$ deg and $l \approx -4.9$ deg, reflects the shape of the non-axisymmetric bar/bulge density distribution. These data therefore provide an independent and strong test for the *COBE/DIRBE* density models. Note that the clump giant density maxima along the LOS are insensitive to a possible radial gradient in the ratio of clump giant stars to L-band luminosity.

For the comparison we fold the model LOS density distributions with a gaussian $\exp(-(\Delta\text{mag}^2/2\sigma^2))$, to simulate the intrinsic dispersion of clump giant absolute magnitudes. In the literature values $0.1^m \lesssim \sigma \lesssim 0.3^m$ have been proposed (Stanek et al. (1997), Stanek & Garnavich (1998), Paczynski & Stanek (1998)). See Fig. 3 of Perryman et al. (1997) for an impression of the sharpness of the clump in *V* and Udalski (2000) for an analysis of the metallicity dependence on the mean I-band brightness. We have explored a number of different values for σ between 0.2^m and 0.4^m , and finally decided for $\sigma = 0.3^m$, because with this value our models reproduce best the observations. For each model we need to select two additional parameters, the normalisation of the model density and a shift in magnitudes. These represent the (unknown) conversion factor between model density units and the number density of clump giant stars, and the absolute magnitudes of clump giants. For model 20A we determine these two parameters such that they fit best the observations at $l \approx 5.5$ deg (field M7) and $l \approx -4.9$ deg (field M5).

Figure 12 shows that the LOS distributions of model 20A compare well with the clump giant observations of Stanek et al. Fitting Gaussians to the upper parts of the model curves yields an asymmetry of 0.44^m between the LOS at $l = -4.9$ deg and $l = 5.5$ deg, even somewhat larger than observed. Also the relative peak heights and approximate widths of the model distributions agree with the data within $\sim 10\%$. These are less of a constraint on the bulge shape, however, because they are influenced by other parameters like the density concentration of the bulge and the clump width σ . We remark that the choice of model normalisation factor such that the main difference is in the peak height of Baade’s window distribution is arbitrary; we could also have decided to make a near-perfect fit to Baade’s window distribution and a 10% error in the peak heights of the other two distributions. I.e., the model is slightly more centrally concentrated than the clump giant distribution.

The measured asymmetry in the new model is significantly larger than in the eightfold-symmetric Richardson-Lucy models of Binney et al. (1997) and Bissantz et al. (1997). These models have a maximal asymmetry $\approx 0.27^m$, and generally $\leq 0.2^m$, compared to the Stanek et al. (1994) result of $0.37^m \pm 0.025^m$. As Figure 13 shows, it is also significantly larger than the asymmetry in the model without spiral arms from Section 4.1, which is not a good fit to the clump giant data. In Fig. 13, the magnitude scale for the different models has been chosen so that they all match the observed distribution in field M7. The smaller asymmetry of the model without spiral arms thus becomes apparent as deviations in the peak positions in BW and, in particular, field M5. The spiral model 20A has a greater asymmetry in

the peak positions for these fields because the elongation of its bar is larger, as discussed above.

Fig. 13 also shows a model “20B”, which was obtained by deprojecting the *COBE* data with a modified broad spiral arm model of FWHM 500 pc, and a model “20S”, which is a smoothed version of the standard model with bar angle 20 deg. For the smoothing we have used the algorithm described in Section 3 in the form that preserves the spiral arms. Model 20S shows that small-scale structure in the luminosity model does not influence the model clump giant distributions in these bulge fields significantly. Model 20B is actually a better fit to the amplitudes of the observed distributions than our reference model 20A. However, it does not fit the L-band data as well (see Section 4.3 below).

So far we have considered luminosity models in which the spiral arm component, if present, has a four-armed structure. This is based mainly on observations of gas tracers (see Vallée (1995) and Englmaier & Gerhard (1999)). However, it is unclear whether the MW has two or four stellar spiral arms. In the L-band data the tangent point at $l \approx 50$ deg is not visible. This may point to a two-armed structure; however, this tangent point is also weak in CO, possibly due to the geometry of the LOS through this arm (Dame, private communication). Drimmel & Spergel (2001) argue that the Sagittarius-Carina arm is - at least - weaker than the other arms. Therefore we now ask whether our results on the structure of the bar/bulge depend on the assumption of a four-armed spiral model. We have generated two non-parametric models of the *COBE/DIRBE* L-band data in which a two-armed parametric model was used both for the starting model and the spiral arm penalty term. The bar angle is still assumed to be 20 deg. In the first model, the arms start near the major axis of the bar, and the pitch angle is half that used in the four-armed model above. In the second, we omit the Sagittarius-Carina arm and its counter-arm, the arms start near the minor axis of the bar, and the pitch angle is the same as in the four-armed model. Compared with the four-armed model 20A, both two-armed models found by the algorithm show only minor differences. They fit the *COBE/DIRBE* L-band data equally well as model 20A; the asymmetry in the clump giant LOS distribution peak positions differs by $\lesssim 0.03^m$, the peak heights differ by $\lesssim 12\%$, and the elongation of the bar/bulge differs by $\lesssim 4\%$. It appears therefore that the Scutum-Crux arm is most important for the deprojection of the bar. Thus the assumption of a four-armed spiral model does not significantly bias the results obtained for the structure of the bar/bulge.

We end this section by a short summary of its main results. The first is that inclusion of spiral structure improves the model of the *COBE/DIRBE* L-band data in the sense of removing unphysical structures in the disk plane. Second, in models including spiral structure the bar is more elongated as compared to triaxially symmetric models, and third, this more elongated bar gives a better representation of the observed apparent magnitude distributions of clump giant stars in several bulge fields.

4.3 Constraining the bar angle

In the previous section we have described model 20A for bar angle $\varphi_{\text{bar}} = 20$ deg as our reference model. We will now construct similar models for a variety of bar angles, and

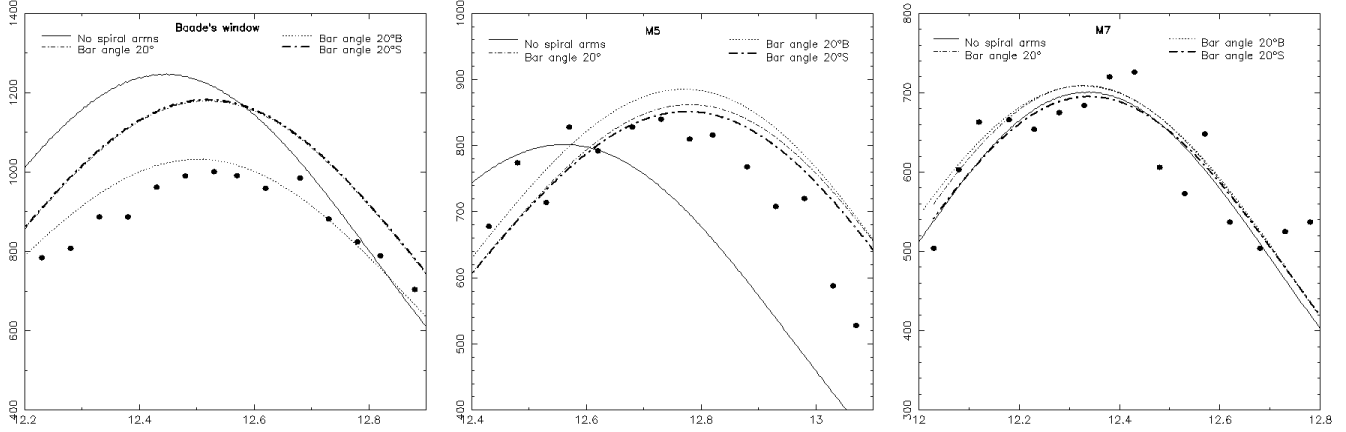


Figure 13. Comparison of observed clump giant line-of-sight distributions with several models, all for $\varphi_{\text{bar}} = 20$ deg: the model without spiral arms of §4.1 (full curve), our reference model 20A with spiral arms (dot-dashed), a similar model with broad spiral arms (20B, dotted), and a smoothed version of the reference model (20S, thick dot-dashed).

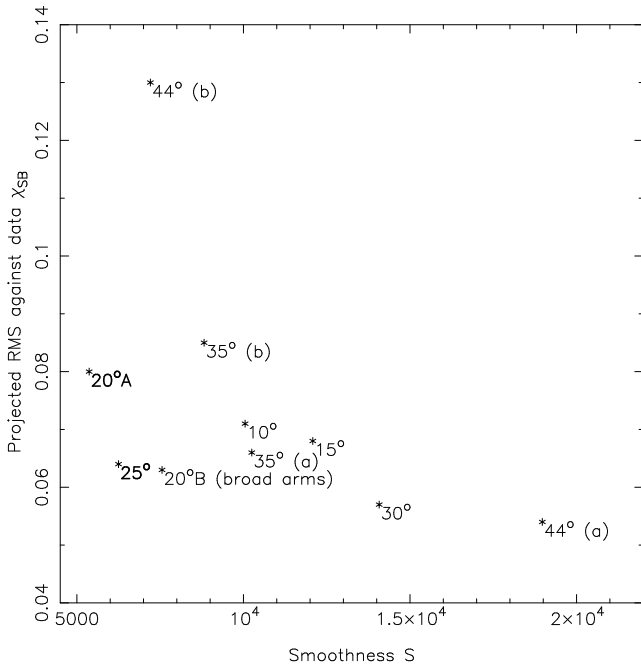


Figure 14. Smoothness parameter S and model RMS χ_{SB} for non-parametric models with spiral arms of the *COBE/DIRBE* L-band data, for bar angles $10 \text{ deg} \leq \varphi_{\text{bar}} \leq 44 \text{ deg}$. Models in the lower left of the diagram both provide a good fit to the surface brightness and are the smoothest. Those printed in bold face are acceptable models in the sense of $F \leq 3$; cf. Section 3. Model 20B for bar angle 20 deg and with broad spiral arms is the only “marginally acceptable” model ($3 < F \leq 4$). Thus bar angles $20 \text{ deg} \leq \varphi_{\text{bar}} \leq 25 \text{ deg}$ are preferred.

use them to constrain the possible range of φ_{bar} . This will also make clear why we selected model 20A. We will compare these models in three different ways. In the first (and weakest) test we use the quality of fit of the *COBE* data for the best-fit *parametric* models used as starting models in the non-parametric deprojections. In the second test we compare the non-parametric models themselves, using the F -criterion of Section 3 which measures a combination of

quality of fit to the data and model smoothness. Finally, the third test uses the distribution of clump giant apparent magnitudes along the LOS measured by Stanek et al. ((1994), (1997)).

We have non-parametrically estimated the *COBE* data for bar angles $\varphi_{\text{bar}} = 10 \text{ deg}, 15 \text{ deg}, 20 \text{ deg}, 25 \text{ deg}, 30 \text{ deg}, 35 \text{ deg}, 44 \text{ deg}$, using the standard four-armed spiral model, and additionally for $\varphi_{\text{bar}} = 20 \text{ deg}$ using a model with broad spiral arms of FWHM 500 pc. In each case we started the iterations from a corresponding parametric best-fit model.

First we analyse these parametric initial models, and find that they fit best the part of the sky dominated by the central bulge/bar, around $|l| \approx 8 \text{ deg}$, $b \approx \pm 5 \text{ deg}$, when the bar angle is $20 \text{ deg} \leq \varphi_{\text{bar}} \leq 30 \text{ deg}$. For other bar angles the models show systematic deviations from the *COBE/DIRBE* L-band data in these regions in (l, b) , symmetric to the galactic equator.

Second we compare the non-parametric models using the F criterion (goodness of fit combined with smoothness), as introduced in Section 3. Their smoothness parameters S and model RMS are shown in Figure 14. Models in the lower left corner give the best fit to the surface brightness and have the highest degree of smoothness. Acceptable models ($F \leq 3$) are the standard model 20A ($\varphi_{\text{bar}} = 20 \text{ deg}$), and the $\varphi_{\text{bar}} = 25 \text{ deg}$ model. The $\varphi_{\text{bar}} = 20 \text{ deg}$ model with broad spiral arms is marginally acceptable ($3 < F \leq 4$). The other models are not satisfactory: they are either too unsmooth or do not fit the SB data well. We illustrate the trade-off between goodness of fit and smoothness in these cases with two models for $\varphi_{\text{bar}} = 35 \text{ deg}$ and $\varphi_{\text{bar}} = 44 \text{ deg}$, obtained with different smoothness penalty parameters λ . One of these is clearly not smooth, and the other is smooth but fits the *COBE* data poorly. We conclude that bar angles $20 \text{ deg} \leq \varphi_{\text{bar}} \leq 25 \text{ deg}$ are preferred.

Finally, we compare the predicted clump giant line-of-sight distributions of these models with observations by Stanek et al. ((1994), (1997)) in Figure 15. The intrinsic dispersion of clump giant absolute magnitudes is again set to $\sigma = 0.3^m$ (see Section 4.2). The remaining free parameters of the models, that is the normalization and the magnitude

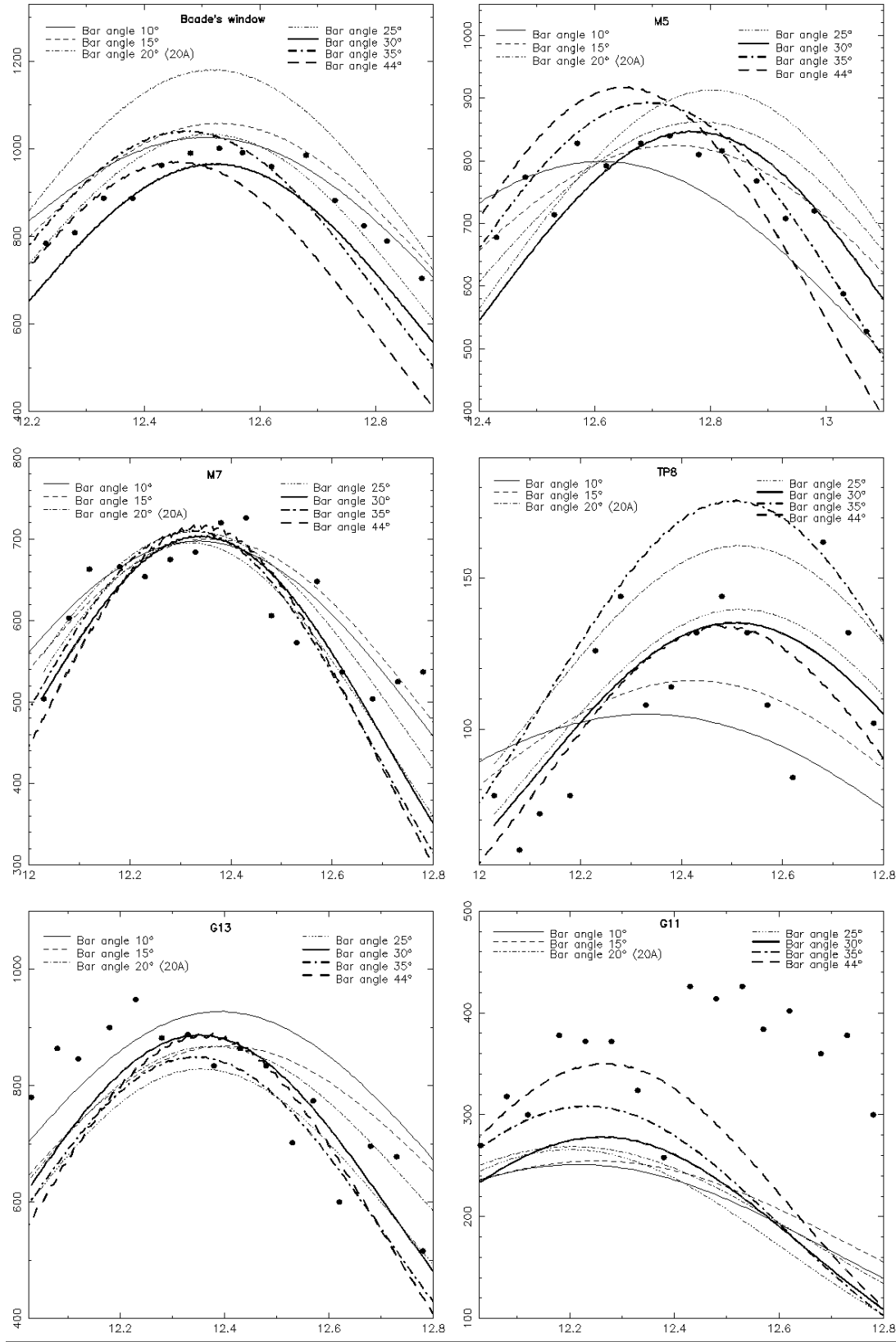


Figure 15. Clump giant distributions for models with different bar angles. For each model, the normalization and shift in the magnitude scale are determined such that the model fits best the data in field M7. The best fit is found for bar angles $\varphi_{\text{bar}} \approx 15 \text{ deg} - 30 \text{ deg}$.

shift, are fixed by optimizing the model fit to the observations in field M7. These parameters are then identical for all fields.

Fig. 15 shows that several models fit the observed clump giant line-of-sight distributions nearly equally well. None of the models fits the observations in field G11 (at $(l, b) \approx (8.2 \text{ deg}, -4.4 \text{ deg})$), probably since these data are strongly influenced by the underlying broad population of stars (the power-law part in the luminosity function fitted by Stanek et al.). The models with $\varphi_{\text{bar}} = 10 \text{ deg}$ and $\varphi_{\text{bar}} = 44 \text{ deg}$ provide inferior fits to the data. The $\varphi_{\text{bar}} = 10 \text{ deg}$ model has wrong peak positions, heights, and widths for fields TP8 (at $(l, b) \approx (-0.1 \text{ deg}, -8.0 \text{ deg})$) and M5, and in Baade's window the peak width is too large. The $\varphi_{\text{bar}} = 44 \text{ deg}$ model shows wrong peak positions in Baade's window and field M5, and a deficit in asymmetry between Baade's window/field M5 and field M7 (for this model the fit can be improved slightly by using a very high intrinsic dispersion $\sigma \gtrsim 0.4^m$). However, this is far above published values, see §4.2). The other models with $15 \text{ deg} \lesssim \varphi_{\text{bar}} \lesssim 30 \text{ deg}$ cannot be distinguished on the basis of the present data.

In summary, a bar angle $20 \text{ deg} \leq \varphi_{\text{bar}} \leq 25 \text{ deg}$ is consistent with all three tests. The clump giant data are consistent with a wider range, $15 \text{ deg} \leq \varphi_{\text{bar}} \leq 30 \text{ deg}$; however, for $\varphi_{\text{bar}} = 15 \text{ deg}$ and $\varphi_{\text{bar}} = 30 \text{ deg}$ we have not been able to find models passing the F-criterion (goodness of fit combined with smoothness). The 20 deg model 20A stands out by its smoothness.

5 MICROLENSING

We will now provide predictions for the microlensing optical depth for our NIR models. The required conversion factor from luminosity density to mass density can be found from fitting the observed terminal velocity curve with a model for the gas flow in the gravitational potential of the bar and disk, assuming spatially constant L-band mass-to-light ratio M/L_L (Bissantz et al. (1997), Englmaier & Gerhard (1999)). In a forthcoming paper (Bissantz, Englmaier & Gerhard, in preparation) we will describe SPH simulations of the gasdynamics in the potentials of the new luminosity models presented in the present work. The value of M/L_L derived from the terminal curve depends somewhat on the precise model parameters, for example, the pattern speed. For the best SPH model it is $M/L_L = 3.9 \times 10^8 M_\odot / \text{CLU}$, and between the various models it varies in the range $3.7\text{--}4.1 \times 10^8 M_\odot / \text{CLU}$, i.e., by $\pm 5\%$. In the following we will use $M/L_L = 3.9 \times 10^8 M_\odot / \text{CLU}$.

With this value, the optical depth towards Baade's window (BW) ($l = 1 \text{ deg}, b = -3.9 \text{ deg}$) for our reference model 20A is $\tau_{-6} = 0.95$ for the full sample of source stars, using $\beta = -1$ in the parametrization of Kiraga & Paczynski (1994) in accounting for a magnitude cut-off. For clump giant sources only it is $\tau_{-6} = 1.39$ in BW ($\beta = 0$). In Figure 16 we present optical depth maps for both cases, predicted from model 20A, over the entire inner Galaxy region. At constant mass normalisation, the range in luminosity density through BW predicted by models 15, 20B, 30 corresponds to an uncertainty in τ of about 10 percent.

The MACHO group has published revised values for the optical depth near Baade's window based on their new

bulge microlensing data. They give an optical depth for all sources, based on 99 events from 3 yr of data, of $\tau_{-6} = 2.43^{+0.39}_{-0.38}$ averaged over 8 fields centred at $l = 2.68 \text{ deg}$ and $b = -3.35 \text{ deg}$ (Alcock et al. (2000a)). From 52 microlensing events with clump giant sources in 5 yr of data, Popowski et al. (2000) give $\tau_{-6} = 2.0 \pm 0.4$ at a mean position $l = 3.9 \text{ deg}$ and $b = -3.8 \text{ deg}$. The corresponding values predicted from model 20A are $\tau_{-6} = 1.10$ at $l = 2.68 \text{ deg}$ and $b = -3.35 \text{ deg}$ ($\beta = -1$), and $\tau_{-6} = 1.27$ for clump giant sources at $l = 3.9 \text{ deg}$ and $b = -3.8 \text{ deg}$ ($\beta = 0$). Figure 17 shows profiles of optical depth along galactic latitude at the mean longitudes of the MACHO observations. The curve for $l = 2.68 \text{ deg}$ shows the optical depth for all sources, and that for $l = 3.9 \text{ deg}$ the optical depth for clump giant sources only, for comparison with the observational results. Both curves illustrate the steep dependence of τ with Galactic latitude.

The optical depth in the new NIR models is about 10% higher than for the eight-fold symmetric RL models of Bissantz et al. (1997). This near agreement between two independent non-parametric models for the COBE/DIRBE data is gratifying. What difference there is mostly comes from the 10% higher luminosity to mass conversion (M/L_L) for the new model. The effects of the structural differences in the new model appear to compensate. On the one hand, there are more lens stars in the new model where the line-of-sight to Baade's window crosses the spiral arms, increasing τ . On the other hand, because the total surface density along this LOS is approximately constant (since specified by the DIRBE SB), the density in the inner bulge is lower than in the models of Bissantz et al. (1997). This decreases the average distance to the sources, and hence τ .

Compared to the observed optical depths, the predictions of the new model are still low. For clump giant sources only, the model is consistent with the preliminary new value (Popowski et al. (2000)) $\tau_{-6} = 2.0 \pm 0.4$ to within 1.8σ . One assumption we have made is that the microlensed source stars are distributed similar to the luminous matter in the Galaxy. This is confirmed by the good agreement of the clump giant distributions predicted from the NIR model with those measured by Stanek et al. ((1994), (1997)). Further evidence that the lensed stars do not contain a significant component far behind the Galactic center (e.g., in the Sagittarius dwarf) comes from the CMD in Fig. 2 of Popowski et al. . With the distribution of source stars known, the predicted optical depth can only be modified significantly if the distribution of lenses is substantially different from that of the sources, i.e., if mass does not follow NIR light.

Associated uncertainties in the NIR model prediction were discussed by Bissantz et al. (1997). There appears to be two main causes for concern: (i) The corrections by Spergel et al. (1996) for dust absorption might conceivably have caused us to overestimate the luminosity in the Galactic plane. In this case, there could be room for some lensing dark mass in front of the bulge fields. (ii) Independently, the L-band mass-to-light ratio might vary with position in the inner Galaxy. Both would have the effect of modifying the mass distribution of the inner Galaxy but, as discussed by Bissantz et al., the effect of this on the optical depth is limited to $\sim 20\%$ because of the constraints from the terminal velocity curve. Together with the 10% spread in the model optical depth discussed above, this implies an uncertainty

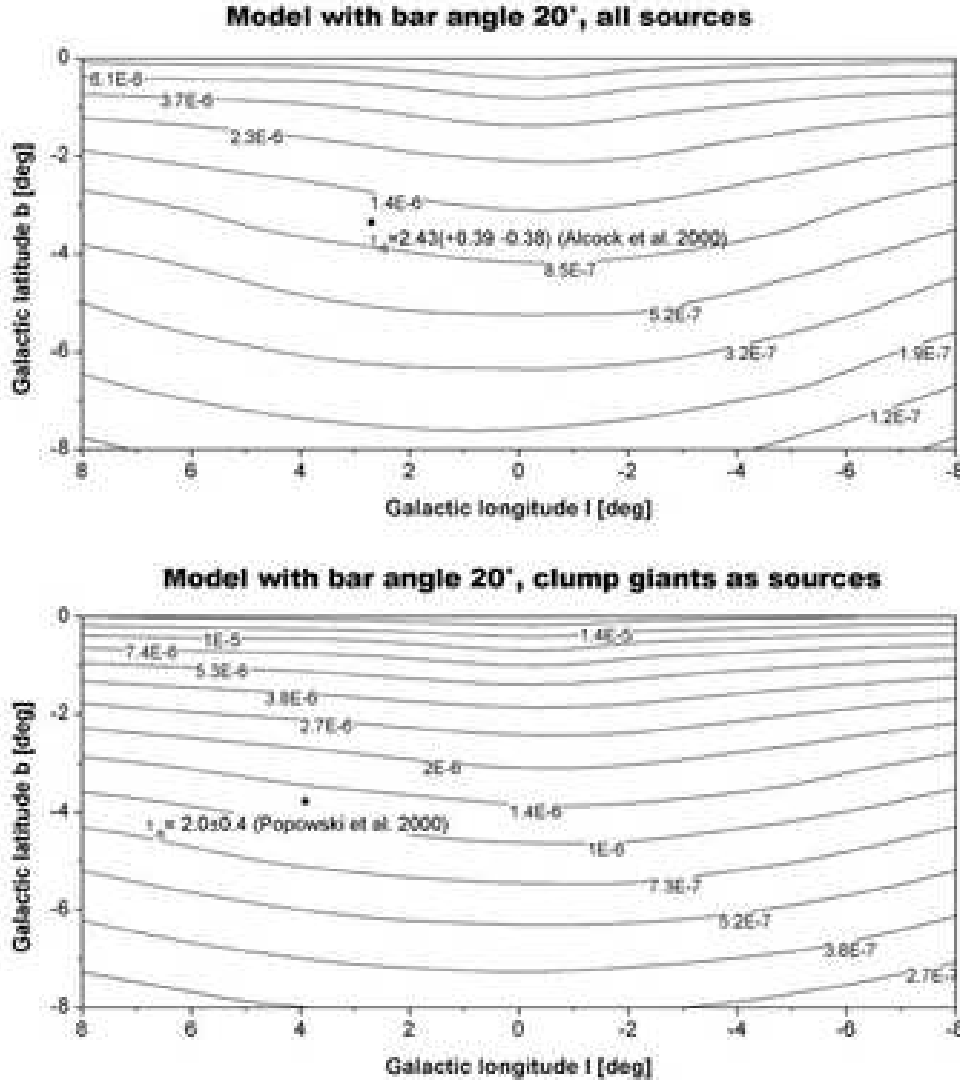


Figure 16. Microlensing optical depth map of our reference model including spiral arms. The model is for bar angle 20 deg. The upper map shows the optical depth for all sources, the lower map for clump giant sources only. The mean positions of the newly published *MACHO* results are indicated in each map.

in the predicted clump giant value of order 0.3, i.e., there is no strong discrepancy with the clump giant measurement of Popowski et al. .

However, the high optical depth of $\tau_{-6} = 2.43^{+0.39}_{-0.38}$ for all sources measured from difference imaging analysis (DIA, Alcock et al. (2000a)) is 3.5σ away from the predicted value of model 20A ($\tau_{-6} = 1.10$), and even after allowing for a 30% uncertainty in the predicted optical depth is still more than 2.5σ discrepant. From the measured optical depth, Alcock et al. deduced $3.23^{+0.52}_{-0.50}$ for bulge sources only, assuming a 25% contribution from disk sources. Binney, Bissantz, & Gerhard (2000) have shown such high optical depths cannot plausibly be reconciled with the Galactic rotation curve and the mass density near the Sun. To underline their argument, to increase the optical depth from $\tau_{-6} = 1.10$ to $\tau_{-6} = 2.43$ for the same distribution of sources and $\beta = -1$, would require an additional surface mass density even at near-optimal distance, $\simeq 4$ kpc, of some $1540 M_{\odot}/\text{pc}^2$, com-

parable to the luminous mass density already present in the NIR mass model ($3636 M_{\odot}/\text{pc}^2$). This may suggest a problem in the interpretation of the DIA measurement, for example, in the correction for amplification bias.

We end this section by commenting on the microlensing contribution of the MW's dark halo. The NIR models with the quoted M/L_L reproduce the Galactic terminal velocity curve out to $\gtrsim 5$ kpc without inclusion of a dark halo (Bissantz, Englmaier & Gerhard, in preparation). If the LSR circular speed is $v_c = 220 \text{ km/s}$ (consistent with $R_0 = 8$ kpc, Reid et al. (1999), Backer & Sramek (1999)), some dark matter is required between 5 kpc and the solar radius, but most of this will be at high latitudes, while the line-of-sight to Baade's window, for example, is within one disk scale-height z_0 in this range of Galactocentric radii. Decreasing the amount of luminous mass in the inner Galaxy in favour of dark matter also does not help even if the dark matter microlenses; this case is included in the $\sim 20\%$ uncertainty

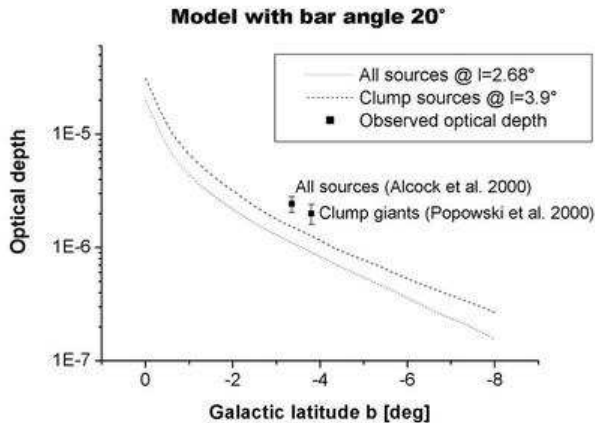


Figure 17. Microlensing optical depth of our reference model at the longitudes of the newly published *MACHO* results, plotted as function of galactic latitude. The observations are indicated in the figure. The upper curve shows the optical depth for clump giant sources, the lower curve for all sources. Both curves are for the galactic longitude of the published observations for the respective group of sources.

discussed above. Moreover, from the LMC microlensing results (Alcock et al. (2000b)) we know that at most a small fraction of this dark matter would actually microlense, so that this would likely *decrease* the predicted optical depth towards the bulge.

6 SUMMARY AND CONCLUSIONS

We have developed a penalized maximum likelihood algorithm that enables us to non-parametrically estimate luminosity densities from surface brightness data. In testing this algorithm with artificial data we found a degeneracy in the bar shape for fixed bar angle, which essentially comes from noise in the data. This implies the existence of a sequence of parametric and non-parametric models that within a given noise level in the data can not be distinguished. For the noise level typical of the *COBE/DIRBE* data, this sequence corresponds to an uncertainty of the in-plane bar elongation η of ± 0.1 and a corresponding variation in the half mass radius $r_{0.5}$ of the bar/bulge of $\pm 20\%$. However, we show that the degeneracy between models on this sequence can be broken by comparing them with the line-of-sight distributions of clump giant stars.

We have non-parametrically estimated luminosity distributions for the *COBE* data, including a model for spiral structure in the disk. This is done in two steps. First we fit a parametric model to the data, then we improve this with the non-parametric algorithm. The initial model contains a spiral arm term proposed by Ortiz & Lépine (1993), which is also used as a prior in a penalty term that is added to the likelihood function in subsequent iterations. Models with spiral arms do not have the unrealistic finger-to-Sun features that are commonly seen in models with an axisymmetric disk, and at the same time fit the surface brightness maps equally well.

We have considered a sequence of models with varying bar angles $10 \text{ deg} \leq \varphi_{\text{bar}} \leq 44 \text{ deg}$. We evaluate these using

both a criterion measuring a combination of the goodness-of-fit to the *COBE* data and the intrinsic smoothness of the luminosity distribution, and the degree to which they account for the asymmetry in the clump giant line-of-sight distributions from Stanek et al. ((1994), (1997)). In this way we find a preferred range $15 \text{ deg} \lesssim \varphi_{\text{bar}} \lesssim 30 \text{ deg}$, with the best models found for $20 \text{ deg} \lesssim \varphi_{\text{bar}} \lesssim 25 \text{ deg}$. In our reference $\varphi_{\text{bar}} = 20 \text{ deg}$ model, the length of the bar is $\approx 3.5 \text{ kpc}$, and its axis ratios are $10 : 3 - 4 : 3$. The in-plane elongation is larger than in previous eightfold symmetric luminosity distributions, because spiral arms make the model appear broader on the sky, thereby requiring a more elongated bar for fixed surface brightness data. The more elongated bar in turn increases the asymmetry in the peak distances of the model's clump giant line-of-sight distributions in the fields observed by Stanek et al. ((1994), (1997)), enabling the new model to reproduce these observations well.

Analysing a model with two spiral arms instead of the four-armed structure of Ortiz & Lépine (1993), we have concluded that our results regarding the structure of the bar/bulge structure and the fit to the clump giant line-of-sight observations do not depend significantly on the assumed spiral arm model, as long as the spiral arm tangent points as seen from the Sun are similar.

The microlensing optical depth in Baade's window for our reference model is $\tau_{-6} \approx 0.95$ for all sources and $\tau_{-6} \approx 1.39$ for clump giant sources only, when the NIR mass-to-light ratio is assumed to be constant and is determined by fitting to the Galactic terminal velocity curve (maximal disk model, Bissantz, Englmaier & Gerhard, in preparation). For clump giant sources at $(l, b) = (3.9 \text{ deg}, -3.8 \text{ deg})$ we find $\tau_{-6} \equiv \tau/10^{-6} = 1.27$, within 1.8σ of the new *MACHO* measurement $\tau_{-6} = 2.0 \pm 0.4$ given by Popowski et al. (2000). The value for all sources at $(l, b) = (2.68 \text{ deg}, -3.35 \text{ deg})$ is $\tau_{-6} = 1.1$, still $> 3\sigma$ away from the published *MACHO* DIA value $\tau_{-6} = 2.43_{-0.38}^{+0.39}$. The dispersion of these τ_{-6} values within our models is $\simeq 10\%$. Because the NIR model is a good representation for the distribution of microlensing sources, the predicted values can only be modified significantly if the distribution of lenses is different from that of the sources. This, however, is constrained because of the good fit of the predicted model terminal curve to the Galactic terminal curve. As we have previously estimated (Bissantz et al. (1997)), this makes it difficult to increase the predicted optical depths by $> 20\%$. Thus the MW disk and bulge must have near-maximal mass-to-light ratio to explain even the clump giant value for the optical depth. As Binney et al. (2000) have argued, optical depths as high as the DIA value are difficult to obtain by any model that is constrained by the Galactic rotation curve and local disk density.

REFERENCES

- Alcock C., et al., 2000a, *ApJ*, 541, 734
- Alcock C., et al., 2000b, *ApJ*, 542, 281
- Backer D.C., Sramek R.A., 1999, *ApJ*, 524, 805
- Binney J., Bissantz N., & Gerhard O., 2000, *ApJ*, 537, L99
- Binney J., Gerhard O., 1996, *MNRAS*, 279, 1005
- Binney J., Gerhard O., Spergel D., 1997, *MNRAS*, 288, 365
- Bissantz N., Englmaier P., Binney J., Gerhard O., 1997, *MNRAS*, 289, 651
- Blitz L., Spergel D.N., 1991, *ApJ*, 379, 631

- Drimmel R., Spergel D.N., 2001, *ApJ*, 556, 181
 Englmaier P., Gerhard O., 1999, *MNRAS*, 304, 512
 Fux R., 1999, *A&A*, 345, 787
 Gerhard, O.E., 2001, in Funes, J.G., S.J., Corsini E.M., eds, *Galaxy Disks and Disk Galaxies*, ASP Conference Series, 230, 21
 Hammersley, P.L., et al., 1999, *MNRAS*, 308, 333
 Kiraga M., Paczynski B., 1994, *ApJ*, 430, L101
 López-Corredoira M., et al., 2000, *MNRAS*, 313, 392
 Nikolaev S., Weinberg M.D., 1997, *ApJ*, 487, 885
 Ortiz R., Lépine R.D., 1993, *A&A*, 279, 90
 Paczynski B. et al., 1994, *ApJ*, 435, L113
 Paczynski B., Stanek K.Z., 1998, *ApJ*, 494, 219
 Perryman M.A.C., Lindegren L., Kovalevsky J., et al., 1997, *A&A*, 323, L49
 Popowski P., Alcock C., Allsman R.A., et al. 2000, in Menzies J.W., Sackett P.D. eds, *Proc. Microlensing 2000*, ASP Conference Series
 Press W.H., Teukolsky S.A., Vetterling W.T., et al., 1994, “Numerical recipes in C” (2nd ed.), (CUP, Cambridge, New York, Melbourne)
 Reid M.J., et al., 1999, *ApJ*, 524, 816
 Sellwood, J.A., Wilkinson, A., 1993, *Rep. Prog. Phys.*, 56, 173
 Sevenster M.N., 1999, *MNRAS*, 310, 629
 Spergel D.N., Malhotra S., Blitz L., 1995, in Minniti D., Rix H.-W., eds, *Spiral Galaxies in the Near-IR*, Springer, Berlin, p. 128
 Stanek K.Z., Mateo M., Udalski, A., et al., 1994, *ApJ*, 429, L73
 Stanek K.Z., Udalski A., Szymanski M., et al., 1997, *ApJ*, 477, 163
 Stanek K.Z., Garnavich P.M., 1998, *ApJ*, 503, L131
 Udalski A., 2000, *ApJ*, 531L, 25
 Vallee J.P., 1995, *ApJ*, 454, 119
 Weiland J.L., Arendt R.G., Berriman G.B., et al., 1994, *ApJ*, 425, L81
 Weiner B.J., Sellwood J.A., 1999, *ApJ*, 524, 112
 Zhao H., Rich M.R., Spergel D.N., 1996, *MNRAS*, 282, 175
 Zhao H., 2000, *MNRAS*, 316, 418